Supporting Information

Unusual solvent-regulated inversion of metal stereocenter in enantiopure Eu_2L_4 helicate: A new strategy for CPL inversion

Qing Ma,‡ Sen Yin,‡ Ziye Song, Ting Gao, Pengfei Yan, Yanyan Zhou and Hongfeng Li*

Key Laboratory of Functional Inorganic Material Chemistry, Ministry of Education, School of Chemistry and Materials Science Heilongjiang University, 74 Xuefu Road, Harbin 150080, China.
E-mail: lihongfeng@hlju.edu.cn
‡ These two authors contribute equally to this work.

Table of contents

1. Experimental section

1.1 Methods

NMR and ESI-TOF-MS

The ^{1}H NMR, ^{19}F NMR and ^{1}H-^{1}H DOSY spectra were recorded on a Bruker AVANCE III 400 MHz spectrometer. ^{1}H NMR chemical shifts are in ppm relative to tetramethylsilane (TMS): $CDCl_3$ (7.26 ppm for ^{1}H), CD_3CN (1.94 ppm for ^{1}H; 1.32 ppm, 118.26 ppm for ^{13}C). ^{1}H-^{19}F HOESY spectra were recorded on a JNM-ECZ400S/L1 spectrometer.

High-resolution electrospray ionization mass spectrometry (ESI-TOF-MS) were recorded by using a Bruker maXis mass spectrometer. Data analysis was conducted with the Mass-Lynx Data Analysis software (Version 4.1) and simulations were performed with the MassLynx Isotope Pattern software.

FT-IR spectra measurements

FT-IR spectra of all samples were performed with a Perkin Elmer Spectrum One spectrophotometer by using KBr disks in the range of 4000−370 cm^{-1}.

Photophysical behavior

UV-vis spectra were recorded in different solvent ratios ($CH_3CN/CHCl_3$ = v/v, $c = 2.5 \times 10^{-6}$ M) at room temperature in 10 mm light path quartz cuvettes on a PerkinElmer Lambda 25 spectrometer.

Excitation and emission spectra were recorded using an Edinburgh FLS 980 fluorescence spectrometer equipped with a red-sensitive photomultiplier detector (Hamamatsu R928). Excitation spectra were measured in CH_3CN (2.5×10^{-6} M) with quartz cuvettes of 10 mm path length. Emission spectra were measured in different solvent ratios ($CH_3CN/CHCl_3$ = v/v, $c = 2.5 \times 10^{-6}$ M) with quartz cuvettes of 10 mm path length.

Luminescence lifetimes were recorded on a single photon counting spectrometer from Edinburgh Instruments (FLS 980) with a microsecond pulse lamp as the excitation source.

The luminescence quantum yields (Φ) of the samples were recorded at room temperature through an absolute method using an Edinburgh Instruments integrating sphere coupled to the modular Edinburgh FLS 980 fluorescence spectrometer. The absolute quantum yield was calculated using the following expression:

$$\Phi = \frac{\int L_{emission}}{\int E_{reference} - \int E_{sample}} \qquad (S1)$$

Where L_{emission} is the emission spectrum of the sample, collecting using the sphere, E_{sample} is the spectrum of the incident light used to excite the sample, collected using the sphere, and $E_{\text{reference}}$ is the spectrum of the light used for excitation with only the reference in the sphere. The method is accurate within 10%.

$$k_r = \frac{1}{\tau_{rad}} = A_{MD,\,0} n^3 \left(\frac{I_{tot}}{I_{MD}}\right) \qquad (S2)$$

The radiative rate constant (k_r) is proportional to the intensity ratio of total integrated emission of the $^{5}D_0 \rightarrow {}^{7}F_J$ transitions (I_{tot}) to the integrated emission of the $^{5}D_0 \rightarrow {}^{7}F_1$ transitions (I_{MD}). $A_{MD,0}$ (14.65 s^{-1}) is the spontaneous emission probability of the $^{5}D_0 \rightarrow {}^{7}F_1$ transition and n is the refractive index of the medium.

The radiative transition (k_r) values and non-radiative transition (k_{nr}) determine the intrinsic quantum yield (Φ_{Ln}) of Eu^{3+} ion emission as shown in eqn (S3).

$$\Phi_{Ln} = \frac{k_r}{k_r + k_{nr}} = \frac{\tau_{obs}}{\tau_{rad}} \qquad (S3)$$

τ_{obs} is the observed lifetimes. On the basis of the emission decay curves monitored within the $^5D_0 \rightarrow {}^7F_2$ transition. The sensitization efficiencies (η_{sen}) can be calculated.

$$\Phi_{overall} = \eta_{sen}\Phi_{Ln} \qquad (S4)$$

Chiraloptical measurements

CD and CPL experiments were performed on an Olis DM245 spectrometer at room temperature. All samples were dissolved in different solvent ratios ($CH_3CN/CHCl_3$ = v/v, c = 2.5 × 10^{-6} M), and quartz cuvettes with optical pathway of 10 mm were employed. CD spectra were recorded in the range of 250−450 nm in increments of 1 nm, and a slit width of 2 mm for the excitation was utilized. CPL spectra were recorded with a 375 nm laser as light source. The emission of left- and right-handed polarized light were collected in the range of 550−720 nm with the integration time of 1 s and the emission slit width of 0.6 mm.

X-ray crystallography

Crystallographic data of $(NMe_4)_2[Eu_2(\mathbf{L^R})_4]$ is given in Table S4. Single crystals of suitable dimensions of $(NMe_4)_2[Eu_2(\mathbf{L^R})_4]$ was selected for single-crystal X-ray diffraction analysis. Crystallographic data were collected at 140 K on a Xcalibur, Eos, Gemini diffractometer with Mo Kα radiation (λ = 0.71073 Å). The structure was solved by direct methods and refined by the full-matrix least-squares method based on F^2 with anisotropic gthermal parameters for all non-hydrogen atoms by using the SHELXS (direct methods) and refined by SHELXL 2018[1] (full matrix least-squares techniques) in the Olex2 package.[2] The crystallographic data in CIF format were deposited at the Cambridge Crystallographic Data Centre with CCDC Nos. 2353626. These data are available free of charge from the Cambridge Crystallographic Data Centre, 12 Union Road, Cambridge CB21 EZ, UK; fax: (+44) 1223-336-033; or e-mail: deposit@ccdc.cam.ac.uk.

Calculation Details

All DFT calculations are performed using the Gaussian16 Revision C.01 program package.[3] Geometry optimizations under different solvents were conducted by the DFT calculations with PBE0-D3(BJ) functional.[4] Relativistic effective core potential SDD was used for the europium atom, and 6-31G* was adopted for all the other atoms.[5−6] The solvent effects of acetonitrile and mixed solvent were considered by SMD solvation model.[7] All the optimizations were confirmed to be stationary points by the absence of imaginary frequencies. Different from geometry optimizations, for calculating more accurate energy, the basis set of the calculated energy is increased from 6-31G* to 6-311G**/6-311+G** (β-diketone part).[8]

TD-DFT excited states calculations of the ligand anion were carried out using the Gaussian16 Revision C.01 program package. In the process of calculating, the PBE0/ma-TZVP basis set was used.[9] The first 5 monoelectronic excitations were calculated and the transition dipole moment of ligand was visualized using Multiwfn and VMD.[10−11]

1.2 Synthetic of ligands $L^{R/S}$ and helicates $(NMe_4)_2[Ln_2(L^{R/S})_4]$ (Ln = Eu, Gd)

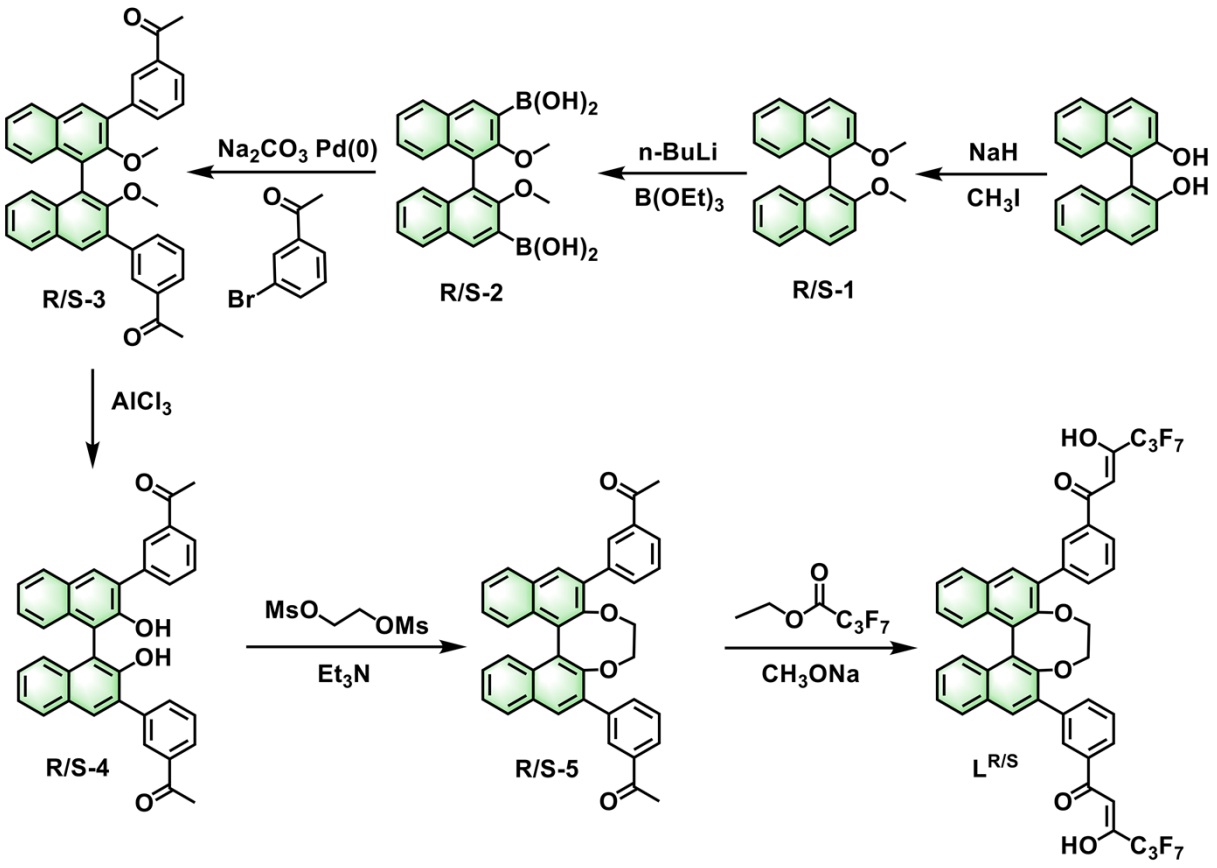

Scheme S1. Synthetic route of ligands $L^{R/S}$.

The intermediates R/S-1 and R/S-2 were prepared according to the previously reported procedures.[12]

Synthesis of (R/S)-3,3′-bis(4-acetylphenyl)-2,2′-dimethoxy-1,1′-binaphthalene R/S-3

Under the N_2 atmosphere, R/S-**2** (2.50 g, 6.22 mmol), $Pd(PPh_3)_4$ (0.50 g, 0.44 mmol) and 3-bromoacetophenone (2.60 g, 13.06 mmol) were placed in a 100 mL Schlenk flask. THF (50 mL) and an aqueous solution of Na_2CO_3 (2.0 M, 25 mL) were added to the mixture and stirred at reflux for 24 h. After cooling to room temperature and extracting with ethyl acetate (3 × 50 mL), the combined organic layers were washed with water and dried over Na_2SO_4, filtered and concentrated under reduced pressure. The crude residue purified by silica gel column chromatography (hexane/ethyl acetate = 3:1) afforded R/S-**3** as a white solid.

R-**3** Yield: 1.68 g, 49%. **^{1}H NMR** (400 MHz, $CDCl_3$): δ 8.27 (s, 2H), 7.93−7.89 (d, *J* = 20.0 Hz, 6H), 7.86−7.84 (d, *J* = 8.0 Hz, 2H), 7.48−7.45 (t, *J* = 8.0 Hz, 2H), 7.36−7.32 (t, *J* = 8.0 Hz, 2H), 7.22−7.19 (t, *J* = 8.0 Hz, 2H), 7.16 (s, 2H), 3.09 (s, 6H), 2.57 (s, 6H) ppm. **ESI-TOF-MS** (m/z): calculated for $C_{38}H_{30}O_4$ $[M + K]^+$ 589.2144, found 589.2106. **IR** (KBr) 740, 1042, 1247, 1350, 1413, 1676, 2932 cm^{-1}. S-**3** Yield: 1.64 g, 48%. **^{1}H NMR** (400 MHz, $CDCl_3$): δ 8.27 (s, 2H), 7.93−7.89 (d, *J* = 20.0 Hz, 6H), 7.86−7.84 (d, *J* = 8.0 Hz, 2H), 7.48−7.45 (t, *J* = 8.0 Hz, 2H), 7.36−7.32 (t, *J* = 8.0 Hz, 2H), 7.22−7.19 (t, *J* = 8.0 Hz, 2H), 7.16 (s, 2H), 3.09 (s, 6H), 2.57 (s, 6H) ppm. **ESI-TOF-MS** (m/z): calculated for $C_{38}H_{30}O_4$ $[M + K]^+$ 589.2144, found 589.2112. **IR** (KBr) 743, 1040, 1241, 1355, 1415, 1675, 2931 cm^{-1}.

Synthesis of (R/S)-3,3′-bis(4-acetylphenyl)-2,2′-dihydroxy-1,1′-binaphthalene R/S-4

R/S-**3** (4.00 g, 7.26 mmol) and anhydrous $AlCl_3$ (3.87 g, 29.07 mmol) were dissolved in 70 mL 1,2-dichloroethane stirred and refluxed for 0.5 h. After cooling to room temperature and extracting with dichloromethane (3 × 50 mL), the combined organic layers were washed repeatedly with water and dried over Na_2SO_4, filtered and concentrated under reduced pressure. The crude residue purified by silica gel column chromatography (hexane/ethyl acetate = 3:1) afforded R/S-**4** as a white solid.

R-**4** Yield: 1.98 g, 52%. **^{1}H NMR** (400 MHz, $CDCl_3$): δ 8.33 (s, 2H), 8.05 (s, 2H), 7.99−7.93 (m, 6H), 7.59−7.56 (t, *J* = 8.0 Hz, 2H), 7.44−7.40 (t, *J* = 8.0 Hz, 2H), 7.37−7.34 (t, *J* = 8.0 Hz, 2H), 7.23−7.21 (d, *J* = 8.0 Hz, 2H), 5.51 (s, 1H), 5.30 (s, 1H), 2.63 (s, 6H) ppm. **ESI-TOF-MS** (m/z): calculated for $C_{36}H_{26}O_4$ $[M + K]^+$ 561.1831, found 561.1807. **IR** (KBr) 745, 1130, 1226, 1247, 1438, 1593, 1676, 3479 cm^{-1}. S-**4** Yield: 2.00 g, 52%. **^{1}H NMR** (400 MHz, $CDCl_3$): δ 8.33 (s, 2H), 8.05 (s, 2H), 7.99−7.93 (m, 6H), 7.59−7.56 (t, *J* = 8.0 Hz, 2H), 7.44−7.40 (t, *J* = 8.0 Hz, 2H), 7.37−7.34 (t, *J* = 8.0 Hz, 2H), 7.23−7.21 (d, *J* = 8.0 Hz, 2H), 5.51 (s, 1H), 5.30 (s, 1H), 2.63 (s, 6H) ppm. **ESI-TOF-MS** (m/z): calculated for $C_{36}H_{26}O_4$ $[M + K]^+$ 561.1831, found 561.1812. **IR** (KBr) 730, 1100, 1232, 1280, 1450, 1610, 1699, 3492 cm^{-1}.

Synthesis of (R/S)-3,3′-bis(4-acetylphenyl)-2,2′-ethylenedioxy-1,1′-binaphthalene R/S-5

R-**4** (5.00 g, 9.58 mmol), 1,2-bis(methanesulfonyloxy)ethane and K_2CO_3 (5.28 g, 38.31 mmol) were dissolved in 50 mL CH_3CN and refluxed for 6 h. After the reaction completed, poured the reaction solution into water and extracted with ethyl acetate (3 × 50 mL). Combined organic layer was and dried over Na_2SO_4, filtered and concentrated solvent under reduced pressure. The crude product was filtered and separated by column chromatography (hexane/ethyl acetate = 5:1) afforded R/S-**5** as a white solid.

R-**5** Yield: 3.41 g, 65%. **^{1}H NMR** (400 MHz, $CDCl_3$): δ 8.36 (s, 2H), 8.09 (s, 2H), 8.00−7.98 (m, 6H), 7.58−7.55 (t, *J* = 8.0 Hz, 2H), 7.49−7.46 (t, *J* = 8.0 Hz, 2H), 7.38−7.30 (m, 4H), 3.65−3.61 (t, *J* = 8.0 Hz, 2H), 3.59−3.55 (t, *J* = 8.0 Hz, 2H), 2.64 (s, 6H) ppm. **ESI-TOF-MS** (m/z): calculated for $C_{38}H_{28}O_4$ $[M + K]^+$ 587.1988, found 587.1965. **IR** (KBr) 710, 1150, 1342, 1415, 1678, 2990 cm^{-1}. S-**5** Yield: 3.25 g, 62%. **^{1}H NMR** (400 MHz, $CDCl_3$): δ 8.36 (s, 2H), 8.09 (s, 2H), 8.00−7.98 (m, 6H), 7.58−7.55 (t, *J* = 8.0 Hz, 2H), 7.49−7.46 (t, *J* = 8.0 Hz, 2H), 7.38−7.30 (m, 4H), 3.65−3.61 (t, *J* = 8.0 Hz, 2H), 3.59−3.55 (t, *J* = 8.0 Hz, 2H), 2.64 (s, 6H) ppm. **ESI-TOF-MS** (m/z): calculated for $C_{38}H_{28}O_4$ $[M + K]^+$ 587.1988, found 587.1959. **IR** (KBr) 742, 1190, 1358, 1472, 1710, 3010 cm^{-1}.

Synthesis of $L^{R/S}$

Sodium methoxide (0.40 g, 7.30 mmol) and ethyl heptafluorobutyrate (1.77 g, 7.30 mmol) were dissolved in ethylene glycol dimethyl ether (20 mL), and then R-**5** (0.50 g, 0.91 mmol) was added and stirred at room temperature for 24 h. The resulting solution was quenched with water and acidified with hydrochloric acid (2.0 M) to pH 2−3. A yellow precipitate was filtered and dried in vacuum.

L^R Yield: 1.44 g, 84.1%. **^{1}H NMR** (400 MHz, $CDCl_3$): δ 15.38 (s, 2H), 8.36 (s, 2H), 8.09 (s, 2H), 8.04−8.02 (d, *J* = 8.0 Hz, 2H), 8.01−7.98 (dd, *J* = 8.0, 3.8 Hz, 4H), 7.64−7.60 (t, *J* = 8.0 Hz, 2H), 7.50−7.48 (t, *J* = 8.0 Hz, 2H), 7.38−7.32 (q, *J* = 8.5, 7.9 Hz, 4H), 6.66 (s, 2H), 3.67−3.55 (m, 4H) ppm. **ESI-TOF-MS** (m/z): calculated for $C_{46}H_{26}F_{14}O_6$ $[M - H]^-$ 939.1506, found 939.1516. **IR** (KBr) 739, 1238, 1459, 1596, 1698, 3420 cm^{-1}. **L^S** Yield: 1.41 g, 82.1%. **^{1}H NMR** (400 MHz, $CDCl_3$): δ 15.38 (s, 2H), 8.36 (s, 2H), 8.09 (s, 2H), 8.04−8.02 (d, *J*

= 8.0 Hz, 2H), 8.01−7.98 (dd, *J* = 8.0, 3.8 Hz, 4H), 7.64−7.60 (t, *J* = 8.0 Hz, 2H), 7.50−7.48 (t, *J* = 8.0 Hz, 2H), 7.38−7.32 (q, *J* = 8.5, 7.9 Hz, 4H), 6.66 (s, 2H), 3.67−3.55 (m, 4H) ppm. **ESI-TOF-MS** (m/z): calculated for $C_{46}H_{26}F_{14}O_6$ $[M-H]^-$ 939.1506, found 939.1523. **IR** (KBr) 762, 1240, 1486, 1563, 1652, 3498 cm^{-1}.

Synthesis of $(NMe_4)_2[Ln_2(L^{R/S})_4]$ (Ln = Eu, Gd)

The ligand $L^{R/S}$ (0.30 g, 0.32 mmol) and tetramethylammonium hydroxide (25% w/w in water, 2.52 mmol) were dissolved in THF (20 mL), and heated until the solution became clear and transparent. $Ln(OTf)_3$ (Ln = Eu, Gd; 0.16 mmol) in 5 mL CH_3CN was added and stirred at room temperature for 24 h, and then the precipitates ware formed after the addition of water. At last, the produce was filtered and dried in vacuum.

$(NMe_4)_2[Eu_2(L^R)_4]$. Yield: 0.26 g, 79%. **ESI-TOF-MS** (m/z): calculated for $C_{184}H_{104}Eu_2F_{56}O_{24}$ **$[Eu_2(L^R)_4]^{2-}$** 2029.1934, found 2029.1933. **$(NMe_4)_2[Eu_2(L^S)_4]$**. Yield: 0.24 g, 74%. **ESI-TOF-MS** (m/z): calculated for $C_{184}H_{104}Eu_2F_{56}O_{24}$ **$[Eu_2(L^S)_4]^{2-}$** 2029.1934, found 2029.1932.**$(NMe_4)_2[Gd_2(L^R)_4]$**. Yield: 0.25 g, 76%. **ESI-TOF-MS** (m/z): calculated for $C_{184}H_{104}Gd_2F_{56}O_{24}$. **$[Gd_2(L^R)_4]^{2-}$** 2034.1965, found 2034.1963. **$(NMe_4)_2[Gd_2(L^S)_4]$**. Yield: 0.25 g, 76%. **ESI-TOF-MS** (m/z): calculated for $C_{184}H_{104}Gd_2F_{56}O_{24}$ **$[Gd_2(L^S)_4]^{2-}$** 2034.1965, found 2034.1964.

1.3 Characterization of intermediates and $L^{R/S}$

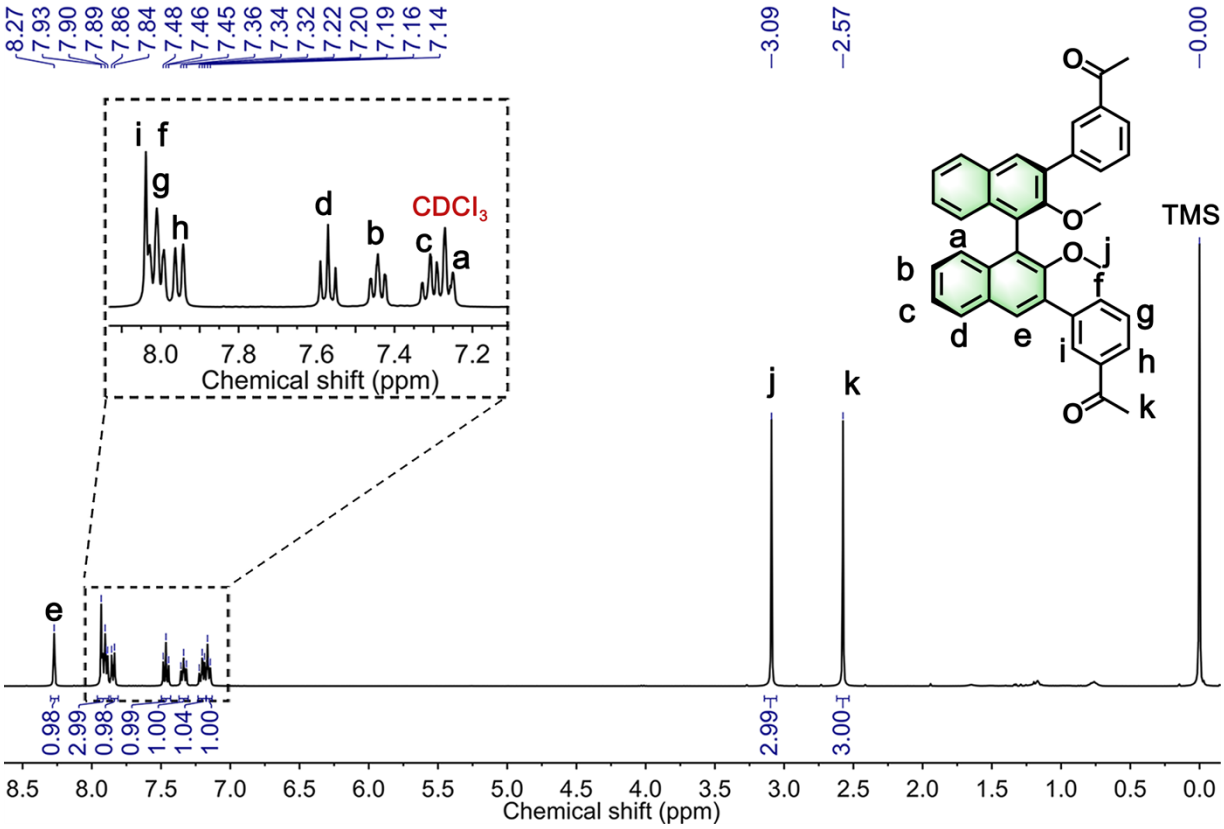

Figure S1. ^1H NMR spectrum (400 MHz, 298 K, $CDCl_3$) of R-**3**.

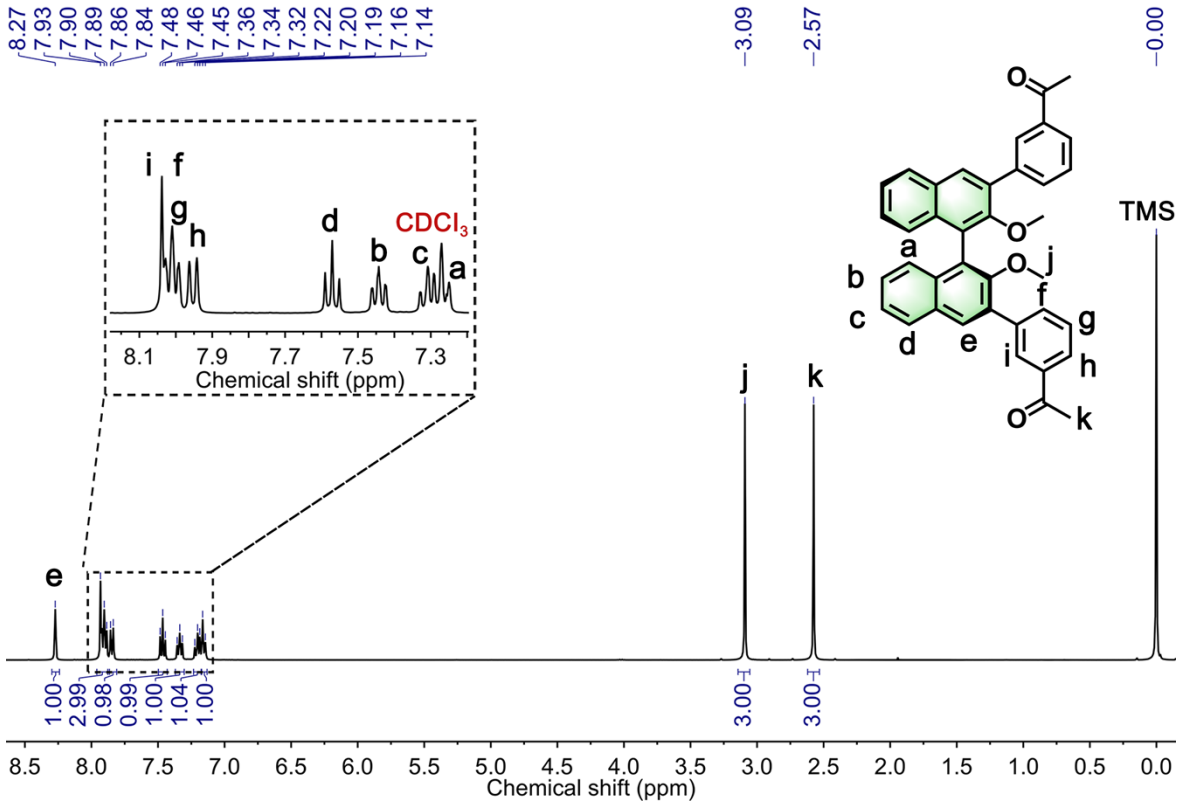

Figure S2. ^{1}H NMR spectrum (400 MHz, 298 K, $CDCl_3$) of S-**3**.

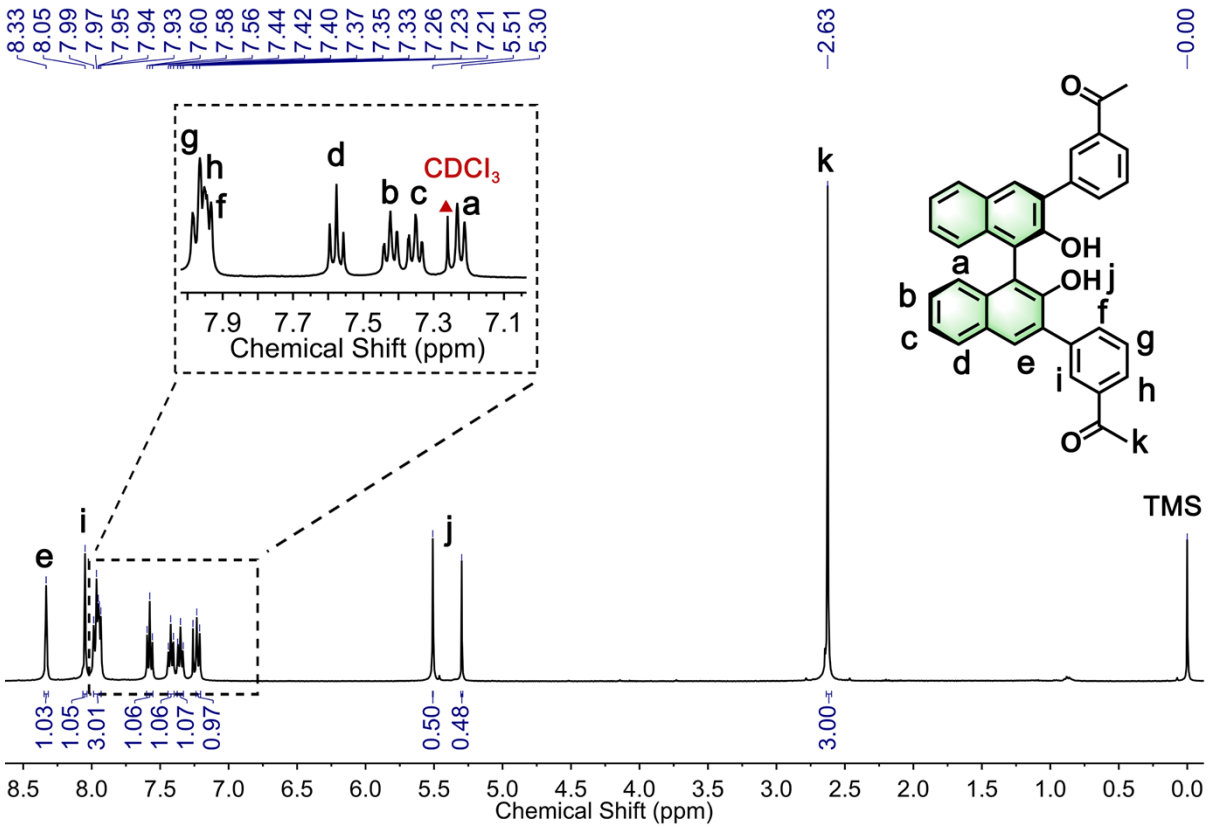

Figure S3. ^{1}H NMR spectrum (400 MHz, 298 K, $CDCl_3$) of R-**4**.

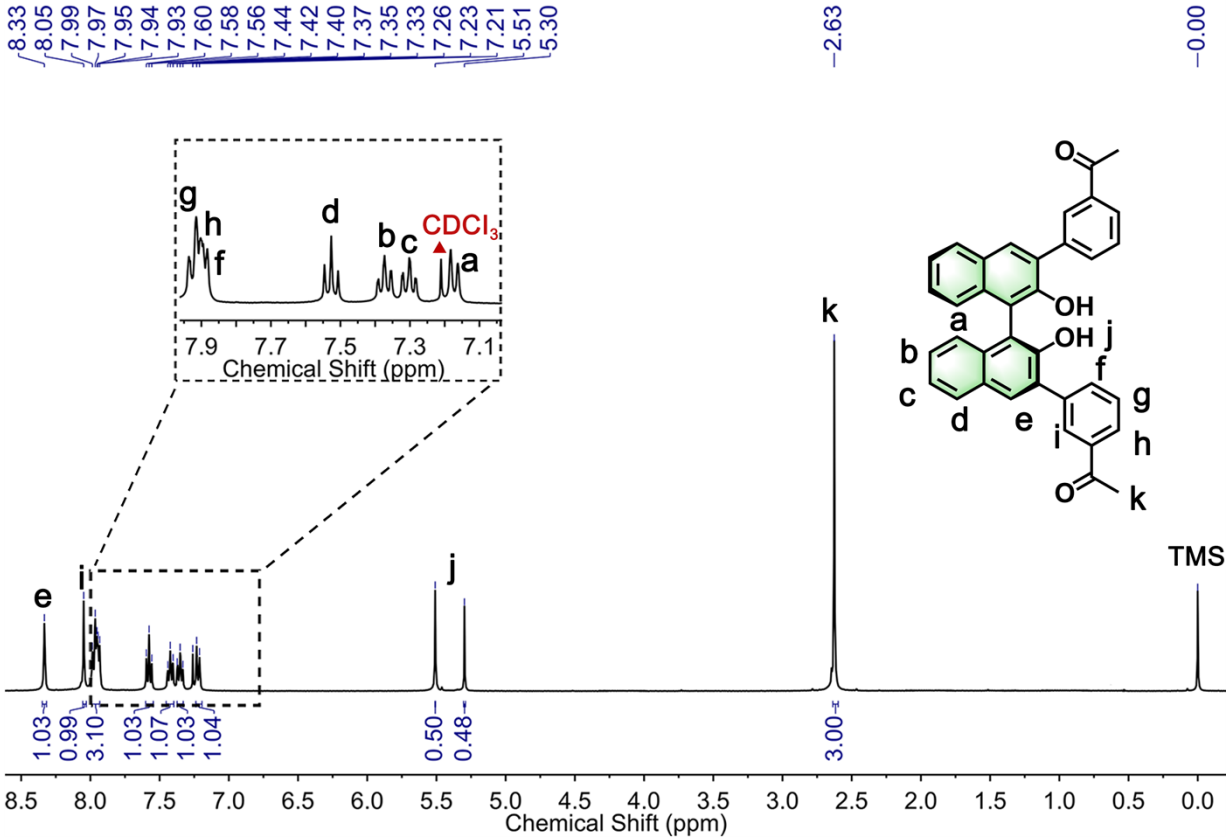

Figure S4. ^{1}H NMR spectrum (400 MHz, 298 K, $CDCl_3$) of S-**4**.

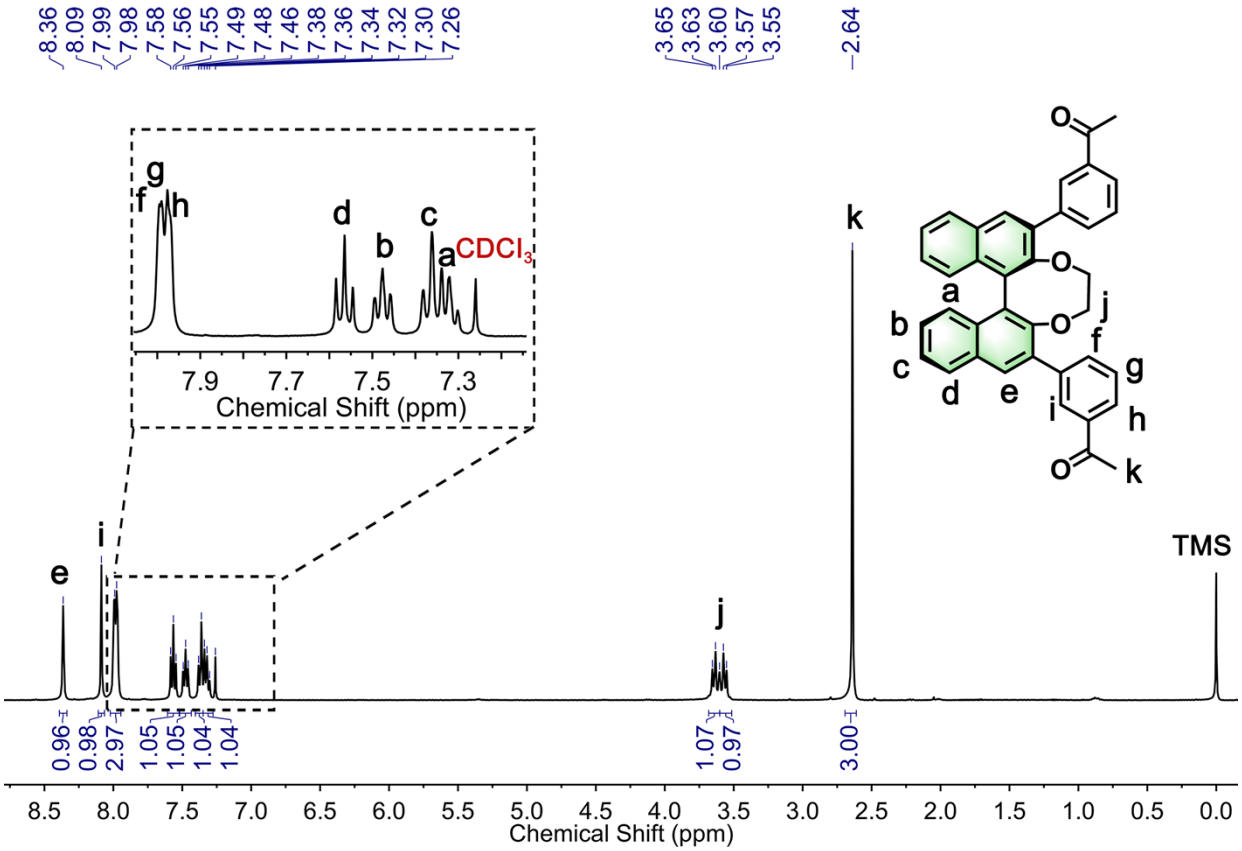

Figure S5. ^{1}H NMR spectrum (400 MHz, 298 K, $CDCl_3$) of R-**5**.

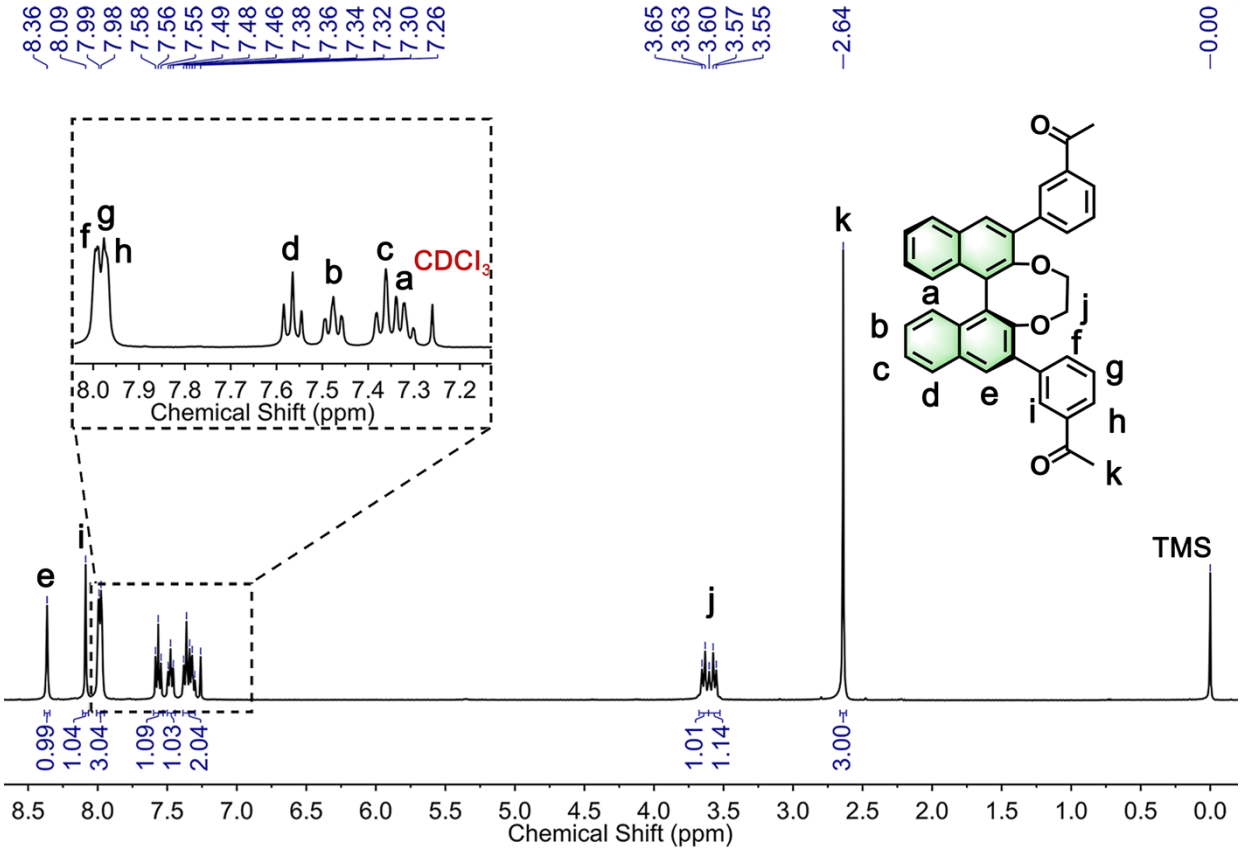

Figure S6. ^{1}H NMR spectrum (400 MHz, 298 K, $CDCl_3$) of S-**5**.

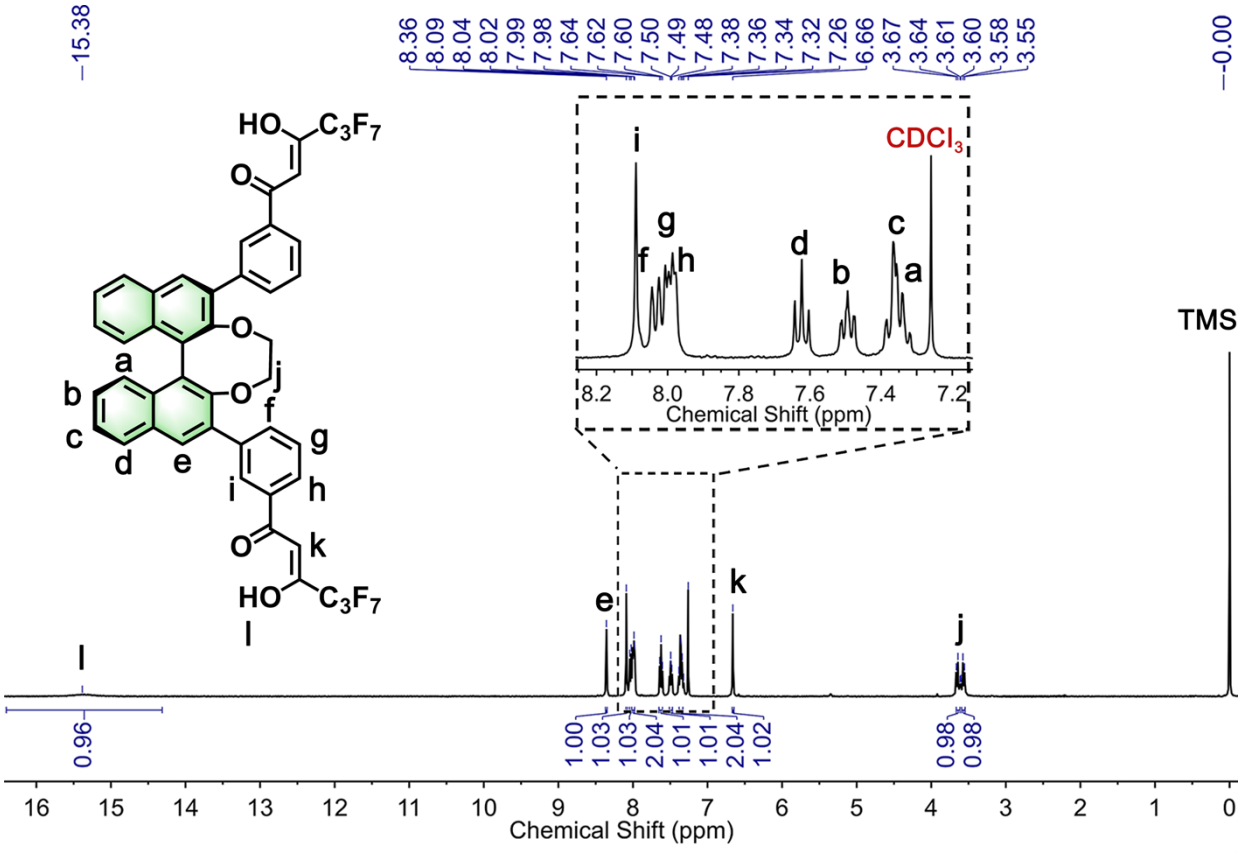

Figure S7. ^{1}H NMR spectrum (400 MHz, 298 K, $CDCl_3$) of $\mathbf{L^R}$.

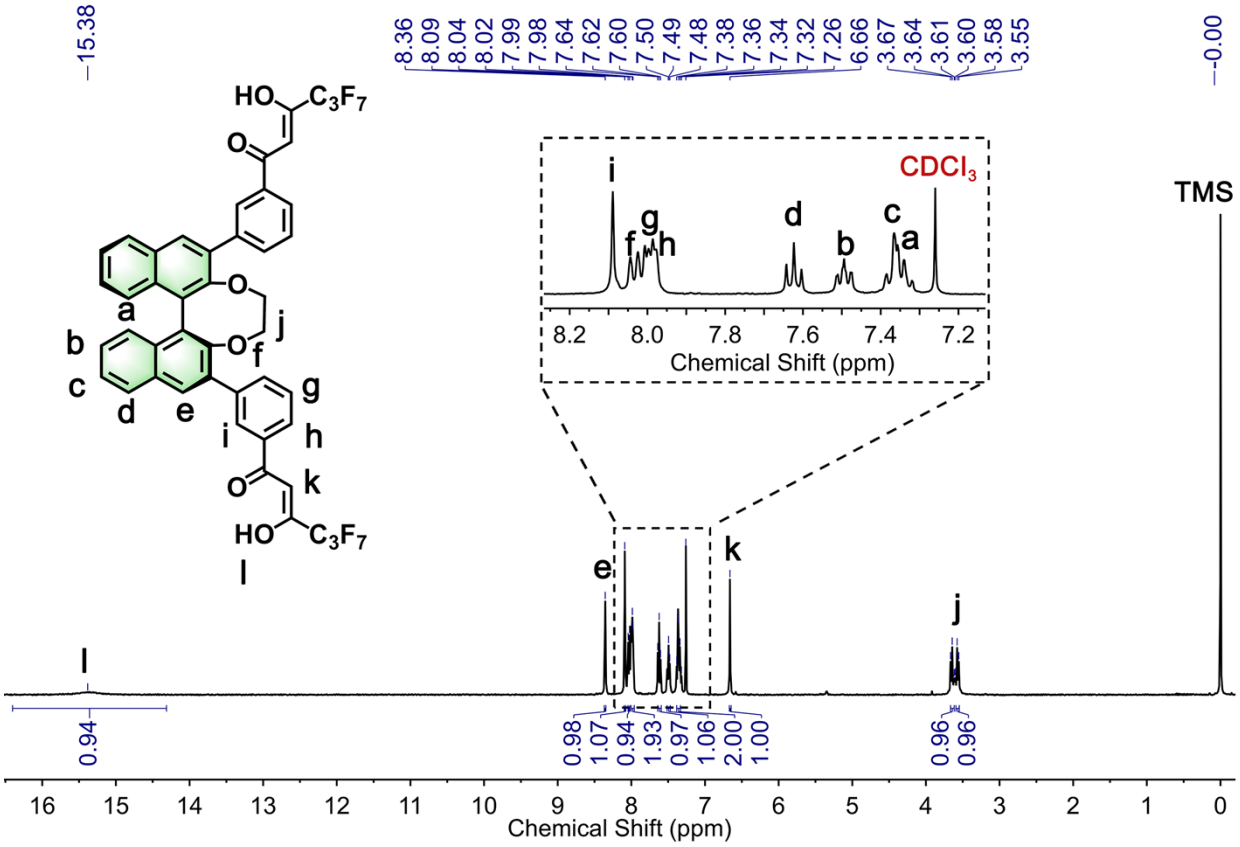

Figure S8. ^{1}H NMR spectrum (400 MHz, 298 K, $CDCl_3$) of $\mathbf{L^S}$.

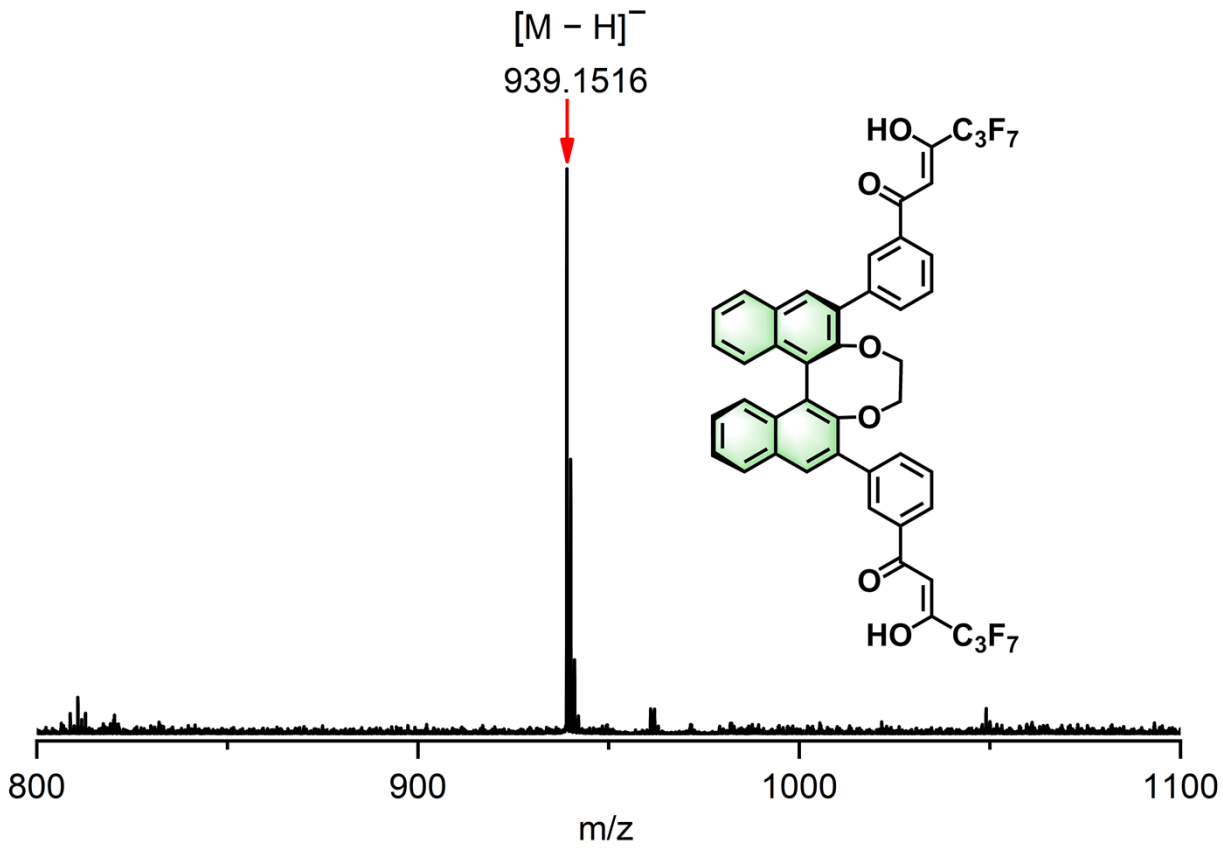

Figure S9. ESI-TOF-MS spectrum of $\mathbf{L^R}$.

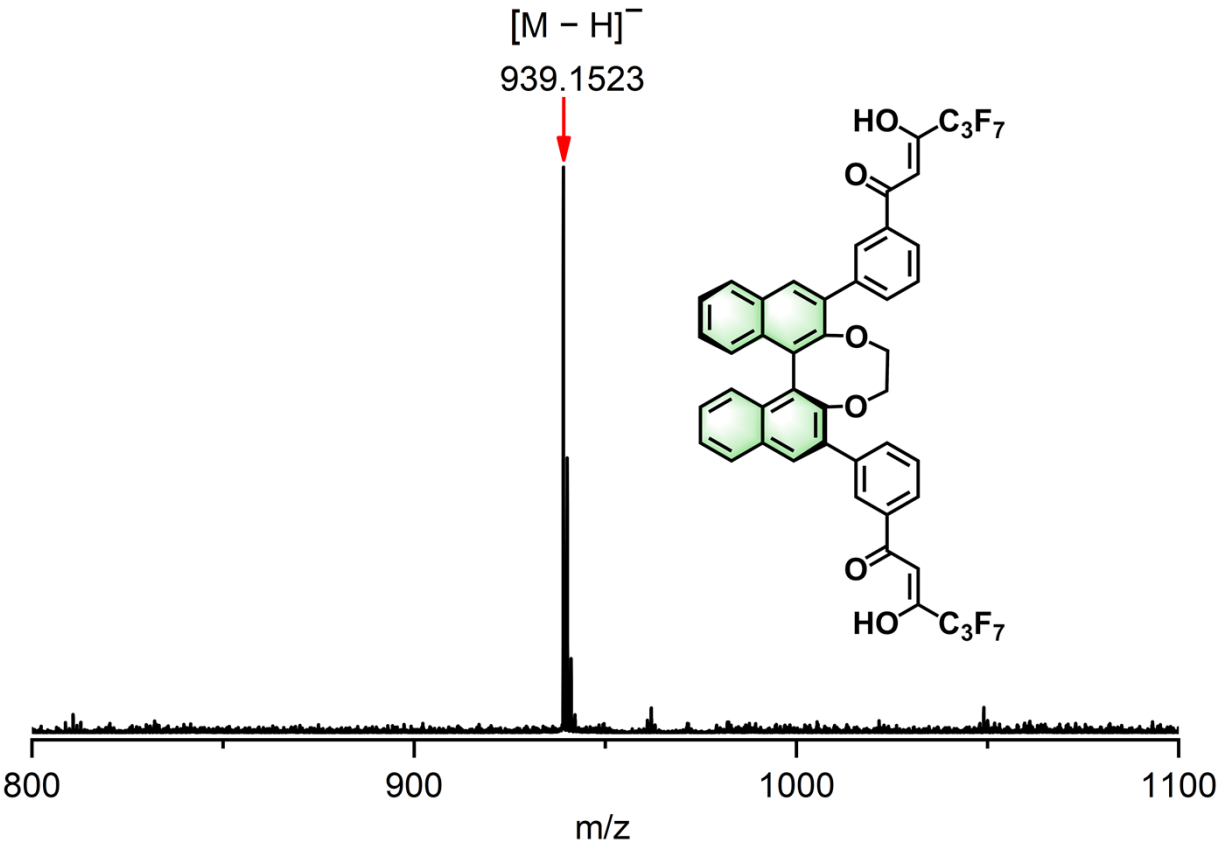

Figure S10. ESI-TOF-MS spectrum of $\mathbf{L}^{S}$.

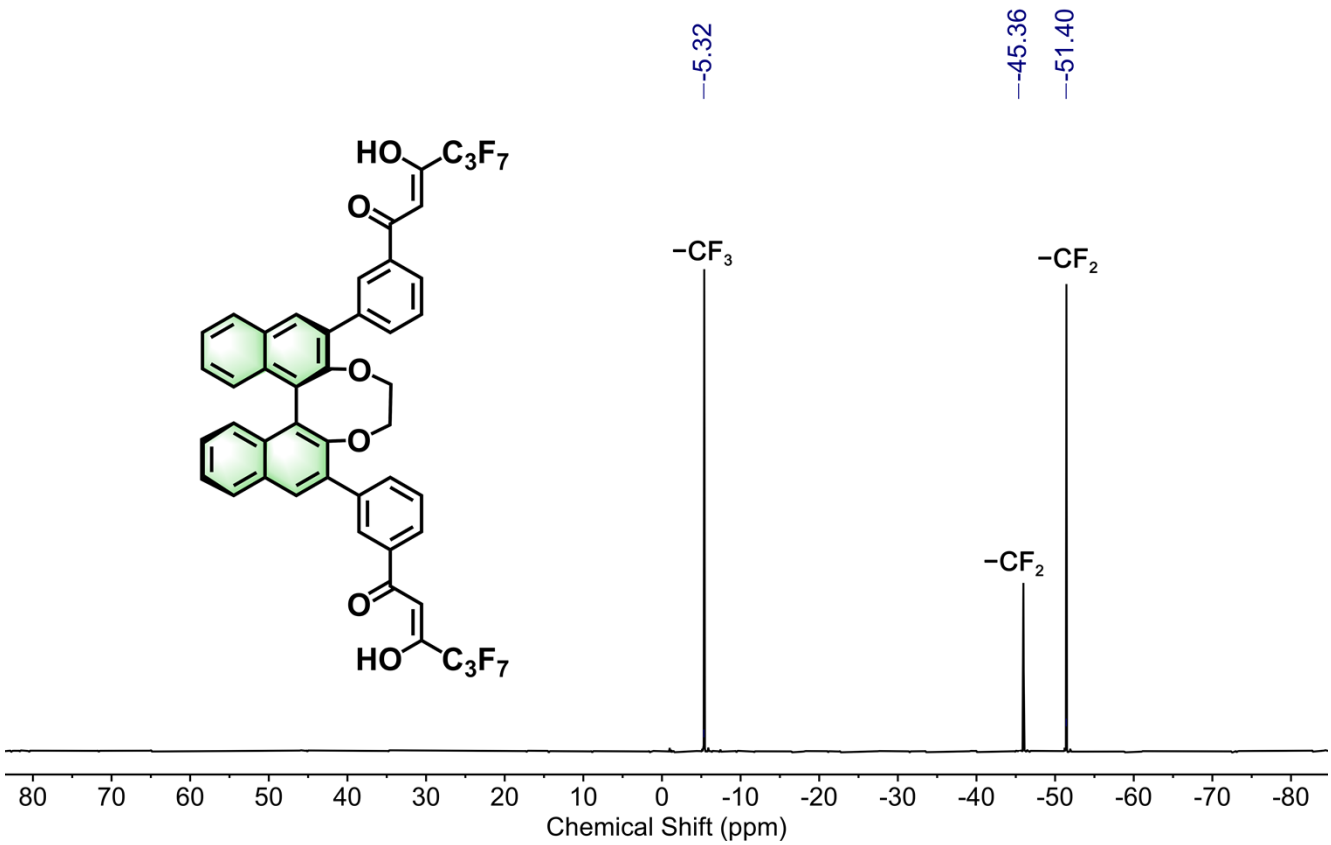

Figure S11. ^{19}F NMR spectrum (376 MHz, 298 K, CD_3CN) of $\mathbf{L}^{R}$.

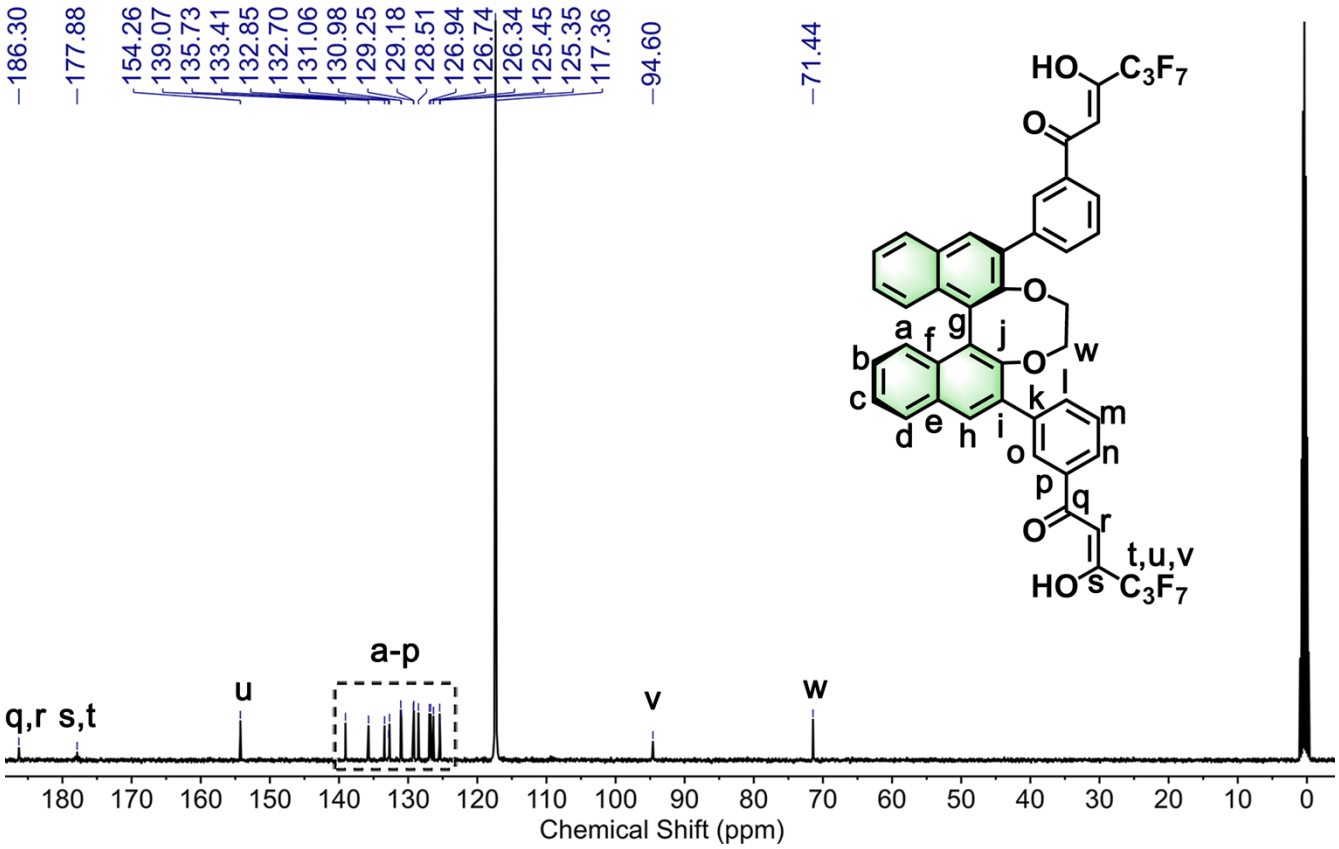

Figure S12. ^{13}C NMR spectrum (101 MHz, 298 K, CD_3CN) of $\mathbf{L^R}$.

1.4 Characterization of $(NMe_4)_2[Ln_2(L^{R/S})_4]$ (Ln = Eu, Gd)

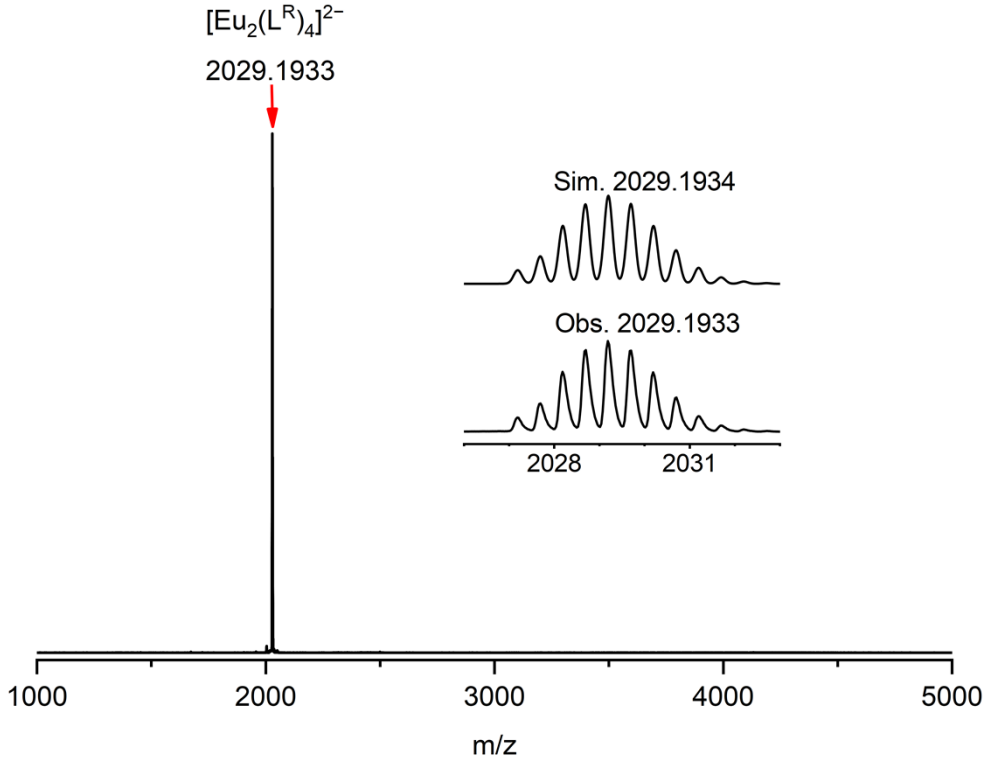

Figure S13. ESI-TOF-MS spectrum of $(NMe_4)_2[Eu_2(\mathbf{L^R})_4]$ in CH_3CN.

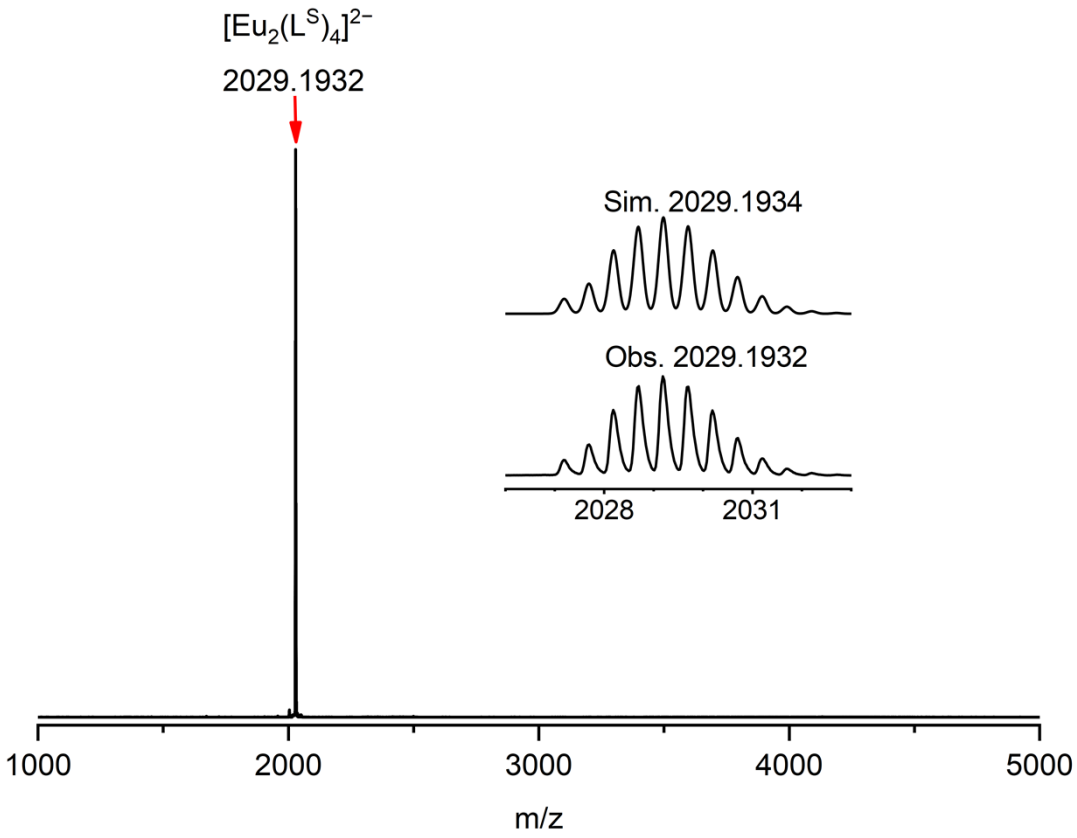

Figure S14. ESI-TOF-MS spectrum of $(NMe_4)_2[Eu_2(\mathbf{L}^{S})_4]$ in CH_3CN.

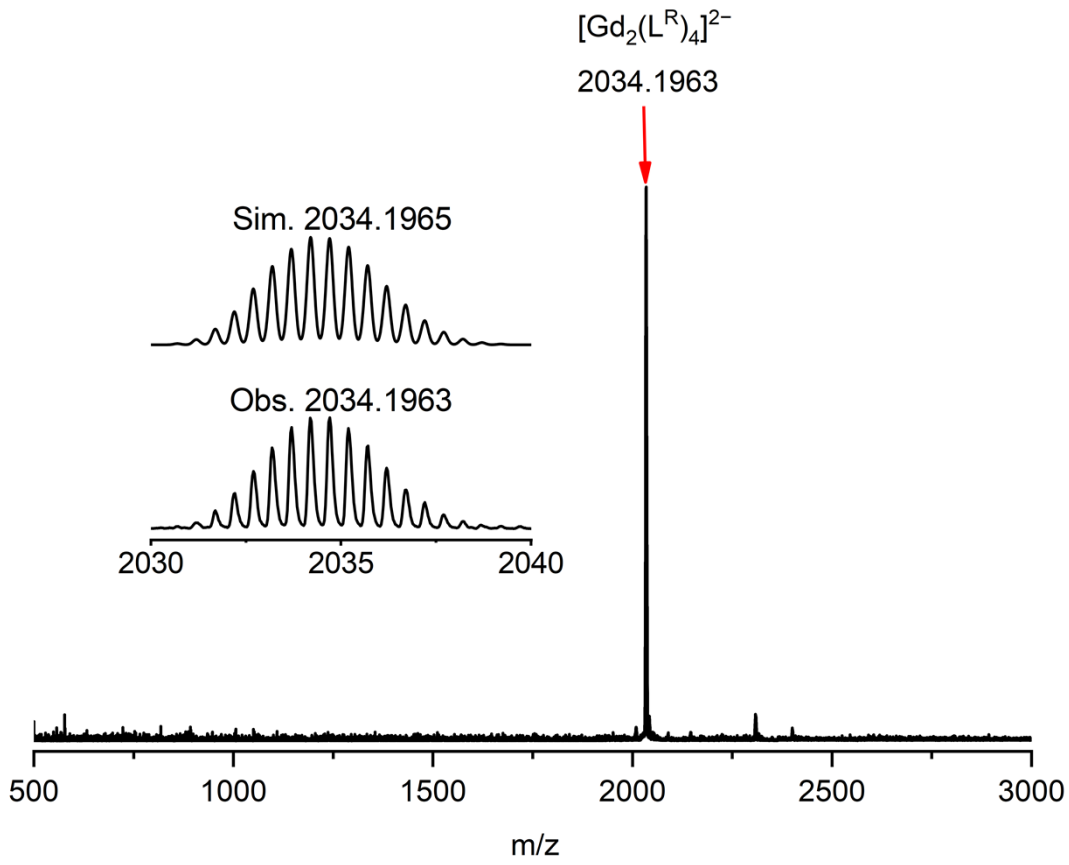

Figure S15. ESI-TOF-MS spectrum of $(NMe_4)_2[Gd_2(\mathbf{L}^{R})_4]$ in CH_3CN.

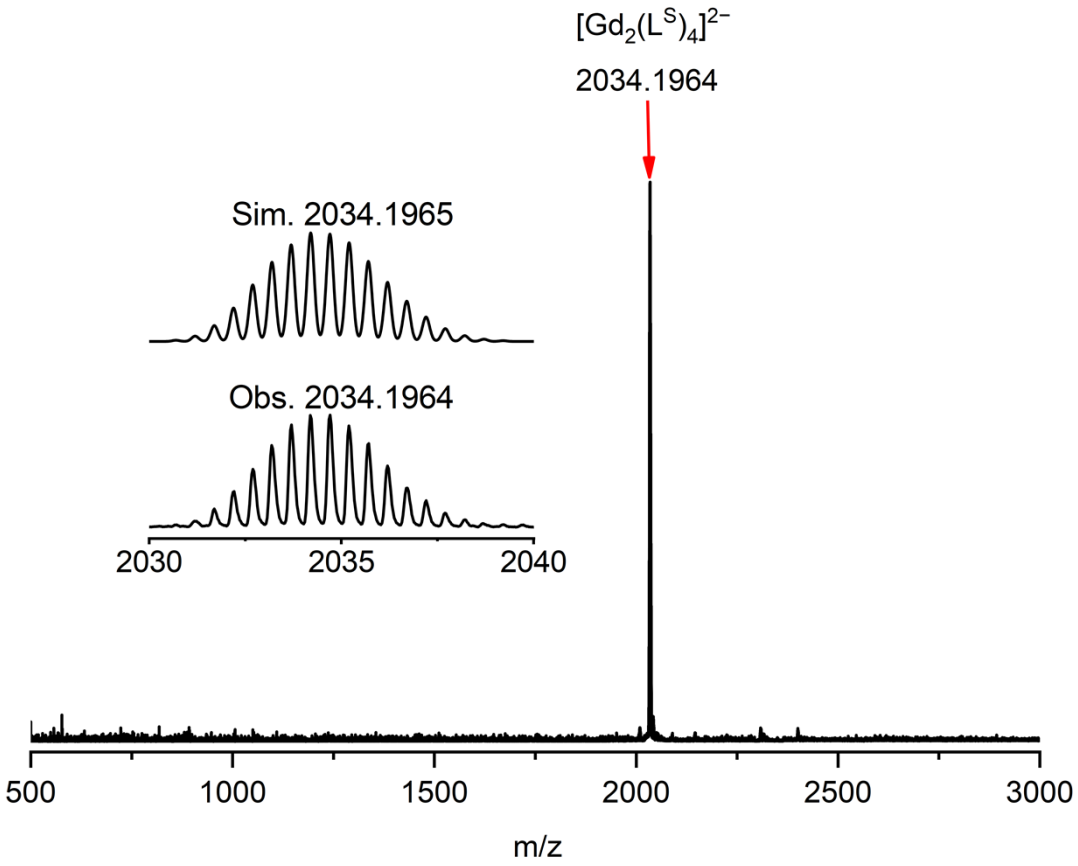

Figure S16. ESI-TOF-MS spectrum of $(NMe_4)_2[Eu_2(\mathbf{L}^S)_4]$ in CH_3CN.

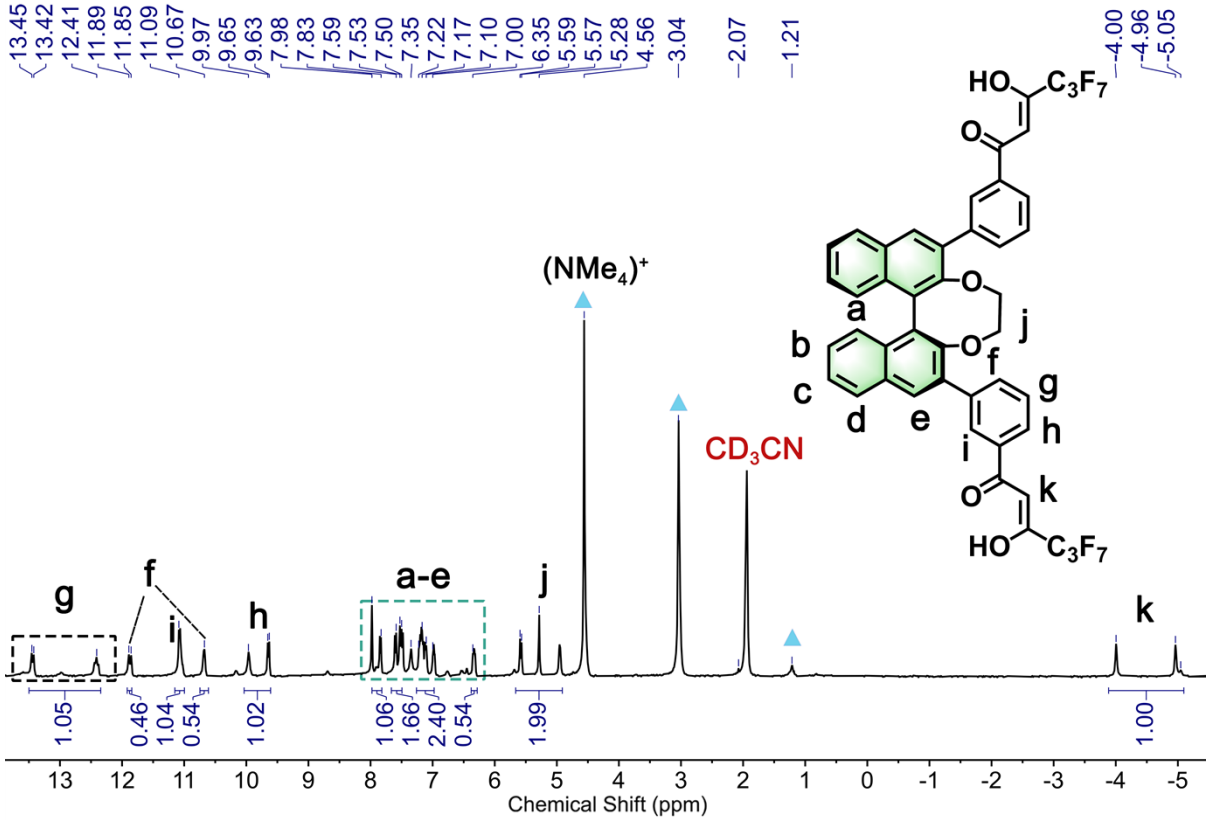

Figure S17. ^{1}H NMR spectrum (400 MHz, 298 K, CD_3CN) of $(NMe_4)_2[Eu_2(\mathbf{L}^S)_4]$.

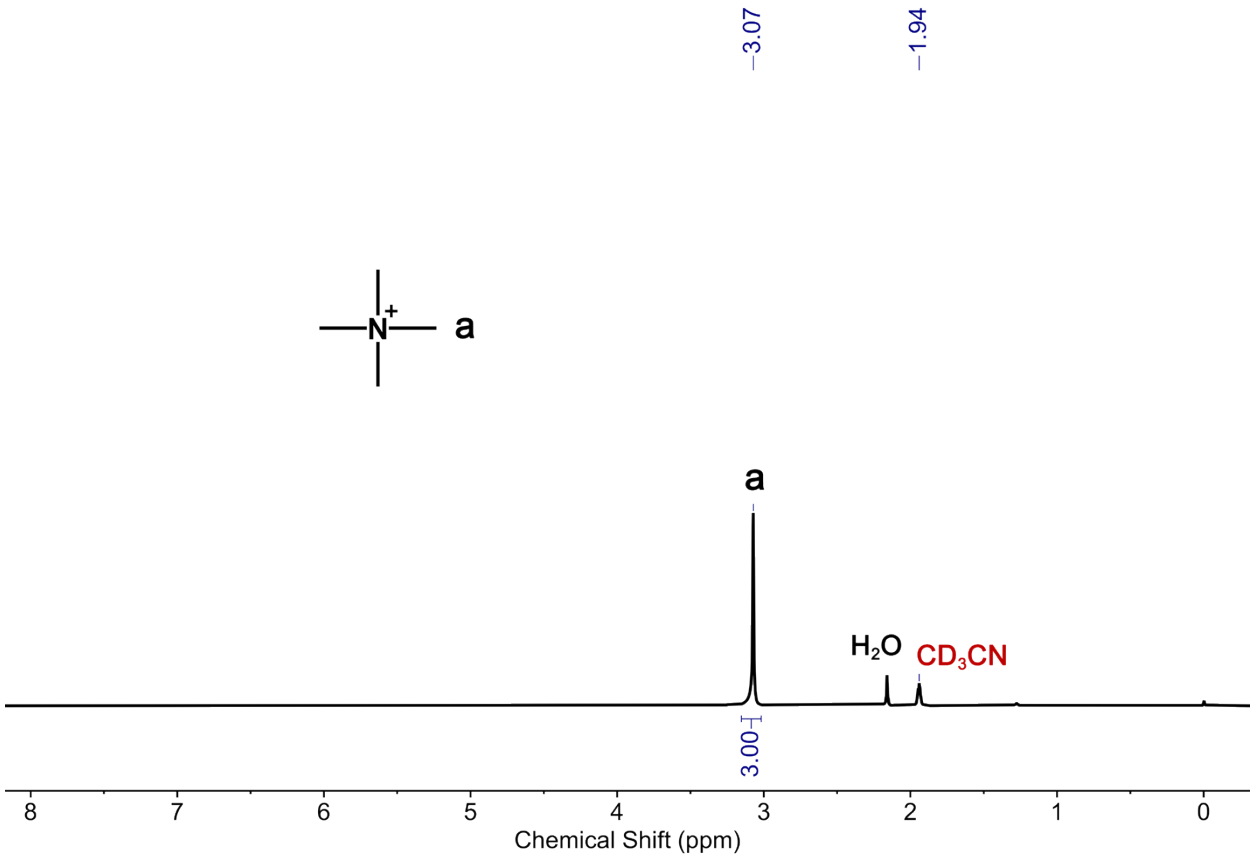

Figure S18. ^{1}H NMR spectrum (400 MHz, 298 K, CD_3CN) of $(NMe_4)OTf$.

2. Study of configuration conversion of $(NMe_4)_2[Eu_2(L^R)_4]$

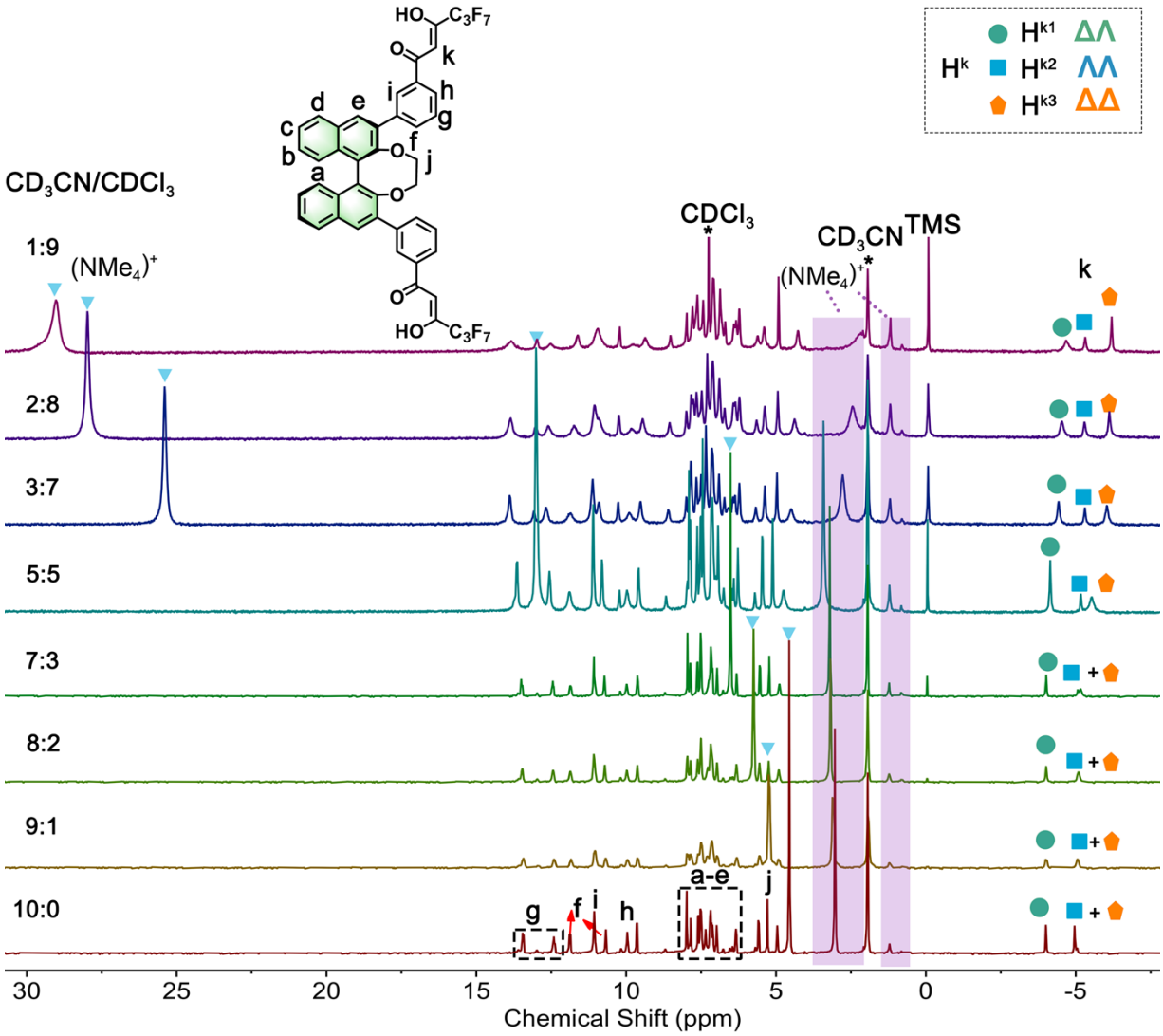

Figure S19. ^{1}H NMR spectra (400 MHz, 298 K) of $(NMe_4)_2[Eu_2(L^R)_4]$ in different solvent ratios ($CD_3CN/CDCl_3$ = v/v).

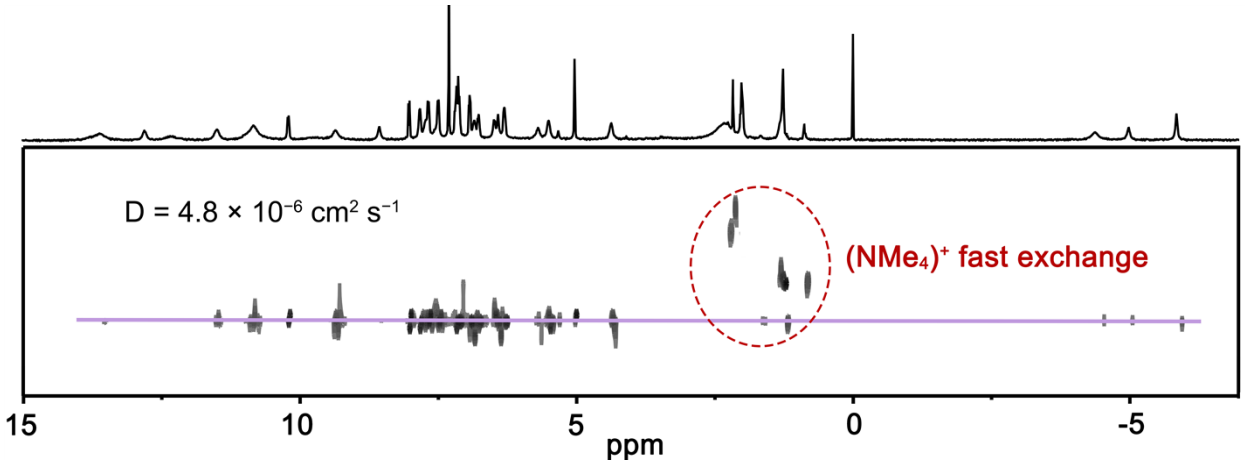

Figure S20. ^{1}H-^{1}H DOSY spectrum (400 MHz, 298 K) of $(NMe_4)_2[Eu_2(L^R)_4]$ in $CD_3CN/CDCl_3$ = 1:9 (v/v).

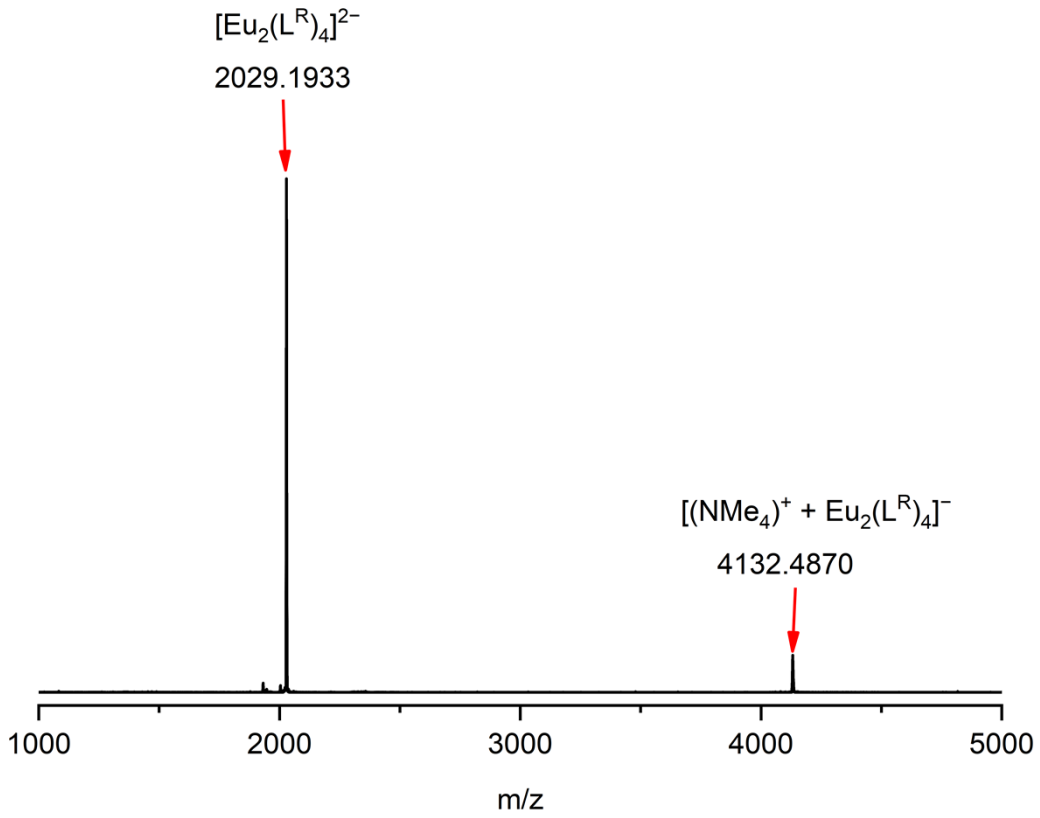

Figure S21. ESI-TOF-MS spectrum of $(NMe_4)_2[Eu_2(\mathbf{L^R})_4]$ in $CH_3CN/CHCl_3$ = 1:9 (v/v).

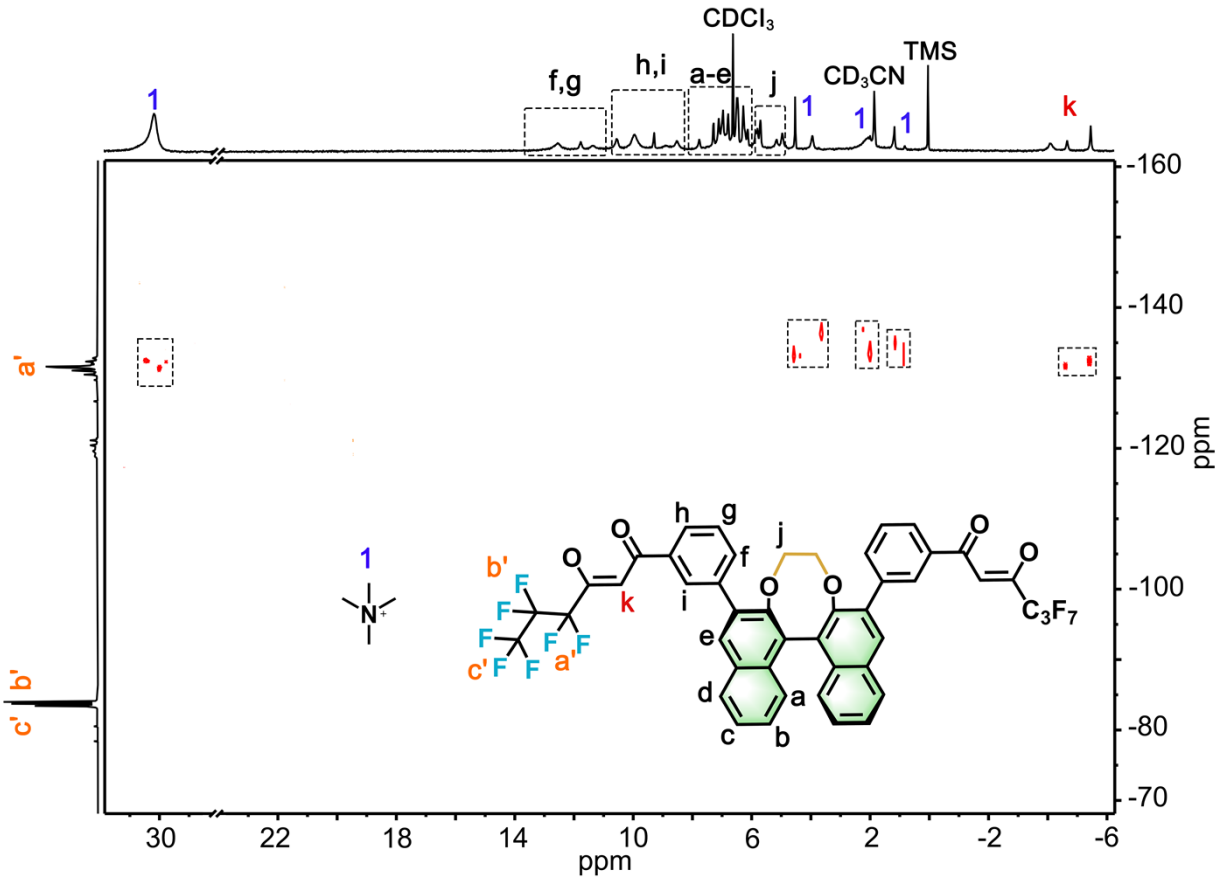

Figure S22. ^{1}H-^{19}F HOESY spectrum (400 MHz, 298 K) of $(NMe_4)_2[Eu_2(\mathbf{L^R})_4]$ in $CD_3CN/CDCl_3$ = 1:9 (v/v).

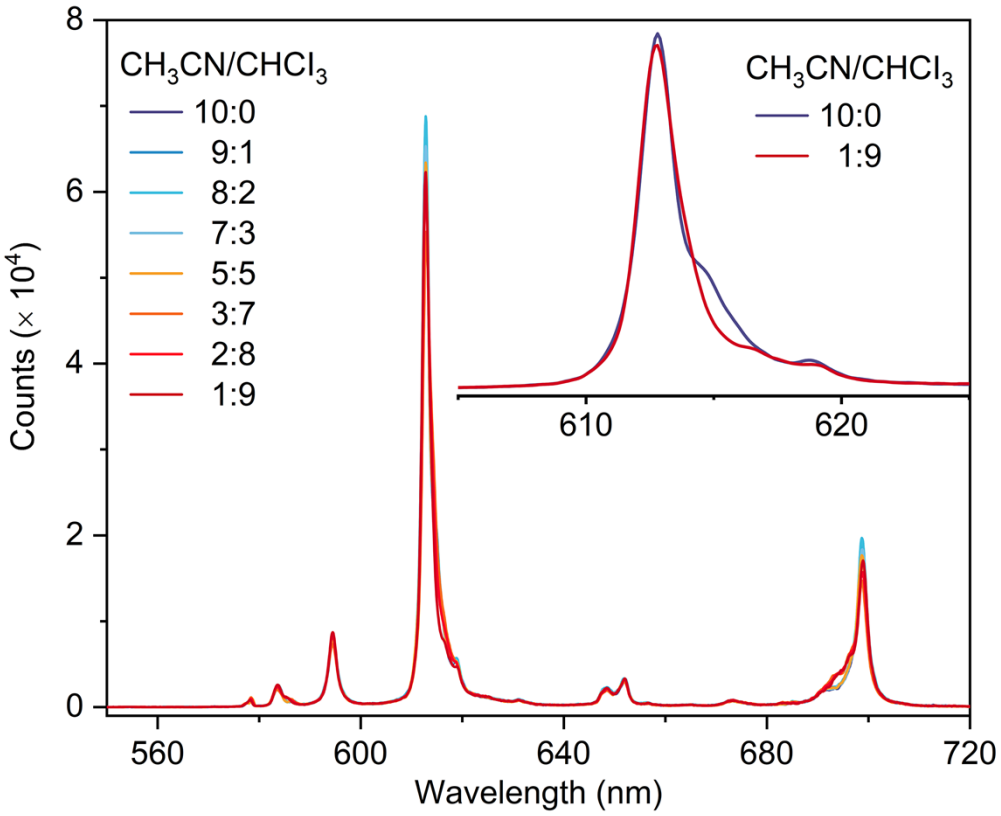

Figure S23. Emission spectra of $(NMe_4)_2[Eu_2(\mathbf{L}^{R})_4]$ in different solvent ratios ($CH_3CN/CHCl_3$ = v/v, $c = 2.5 \times 10^{-6}$ M).

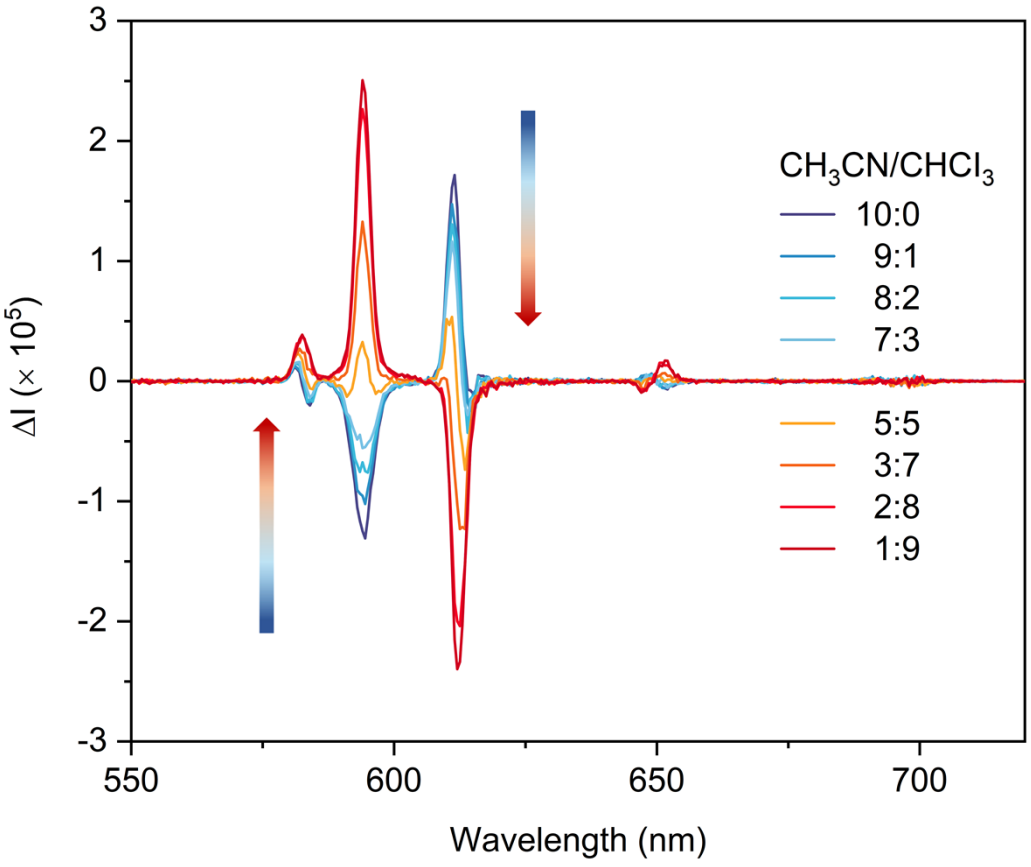

Figure S24 CPL spectra of $(NMe_4)_2[Eu_2(\mathbf{L}^{R})_4]$ in different solvent ratios ($CH_3CN/CHCl_3$ = v/v, $c = 2.5 \times 10^{-6}$ M).

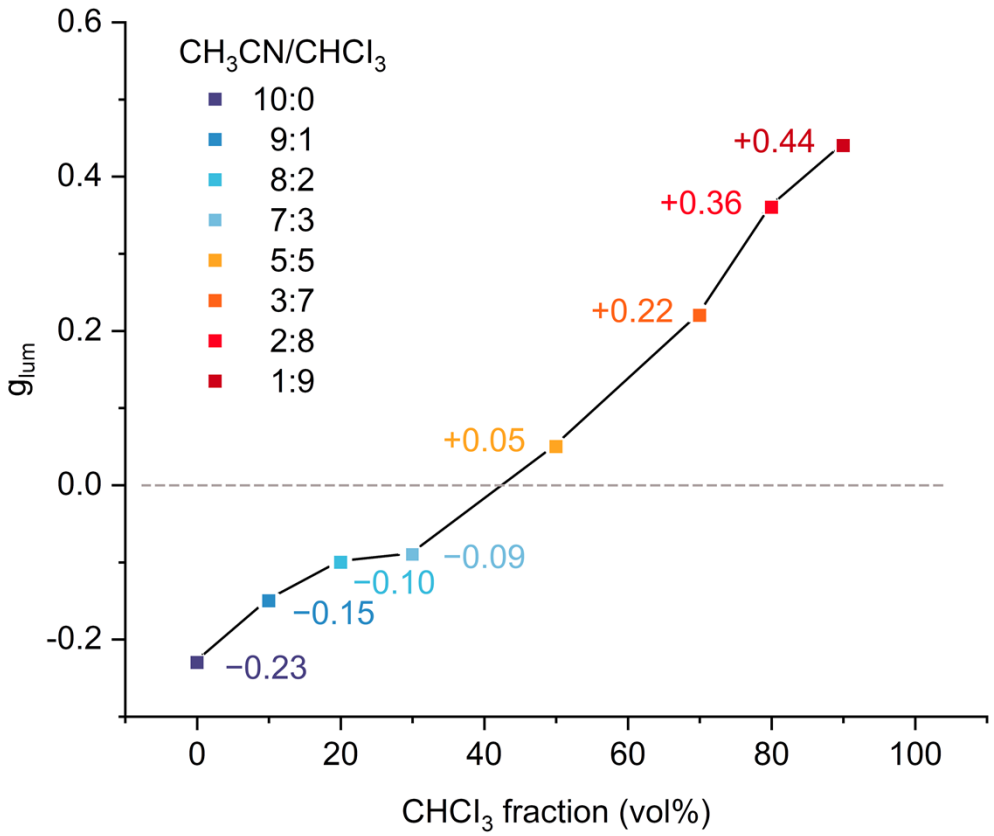

Figure S25. The g_{lum} values of $(NMe_4)_2[Eu_2(\mathbf{L^R})_4]$ in different solvent ratios ($CH_3CN/CHCl_3$ = v/v, $c = 2.5 \times 10^{-6}$ M).

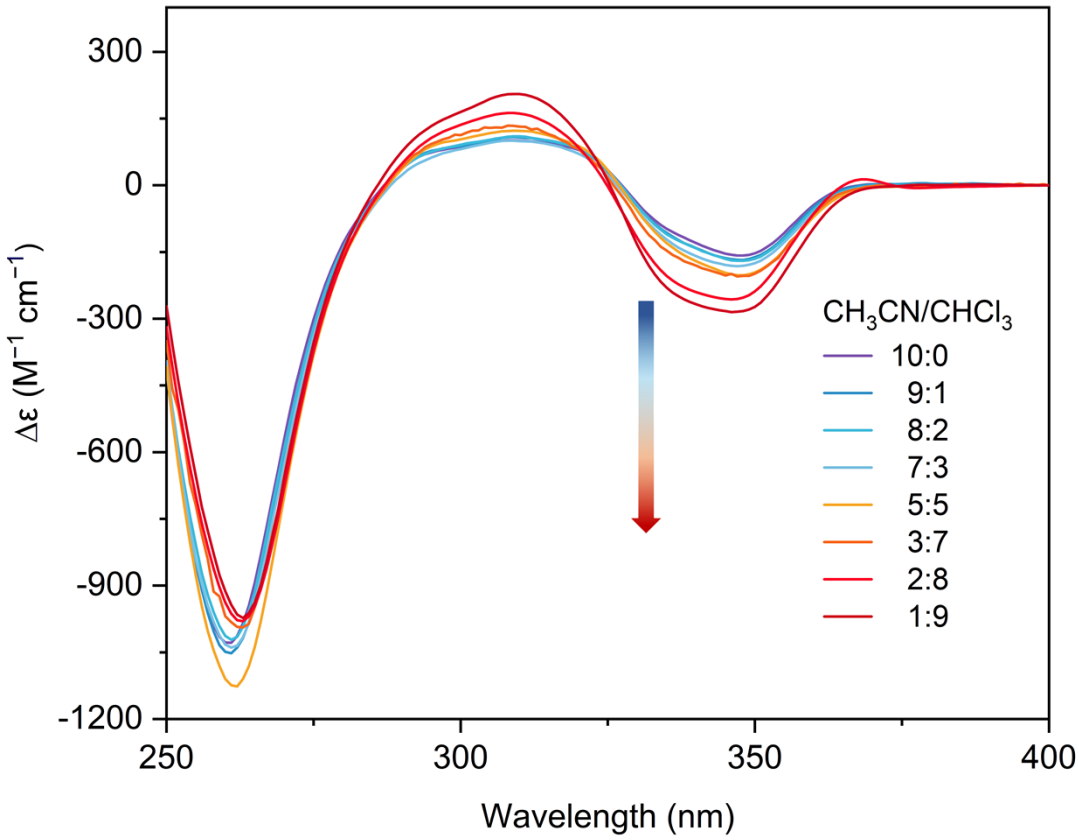

Figure S26. CD spectra of $(NMe_4)_2[Eu_2(\mathbf{L^R})_4]$ in different solvent ratios ($CH_3CN/CHCl_3$ = v/v, $c = 2.5 \times 10^{-6}$ M).

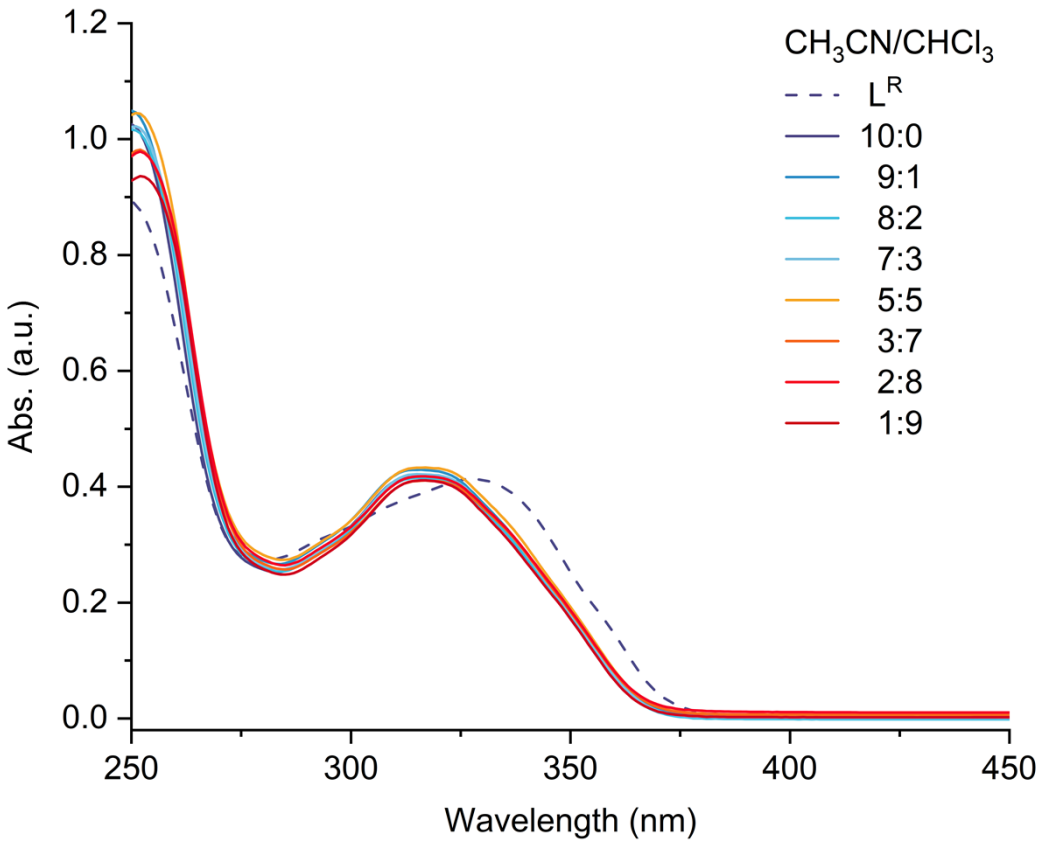

Figure S27. UV-vis spectra of $\mathbf{L^R}$ in CH_3CN (c = 1.0 × 10^{-5} M) and $(NMe_4)_2[Eu_2(\mathbf{L^R})_4]$ in different solvent ratios ($CH_3CN/CHCl_3$ = v/v, c = 2.5 × 10^{-6} M).

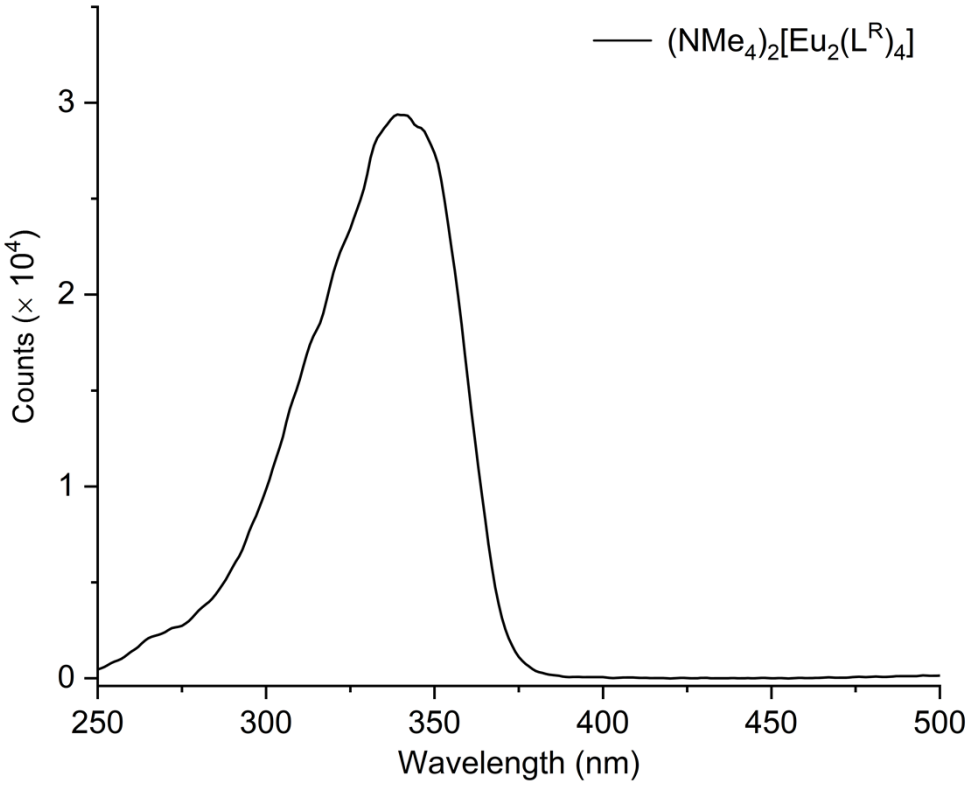

Figure S28. Excitation spectrum of $(NMe_4)_2[Eu_2(\mathbf{L^R})_4]$ in CH_3CN (c = 2.5 × 10^{-6} M).

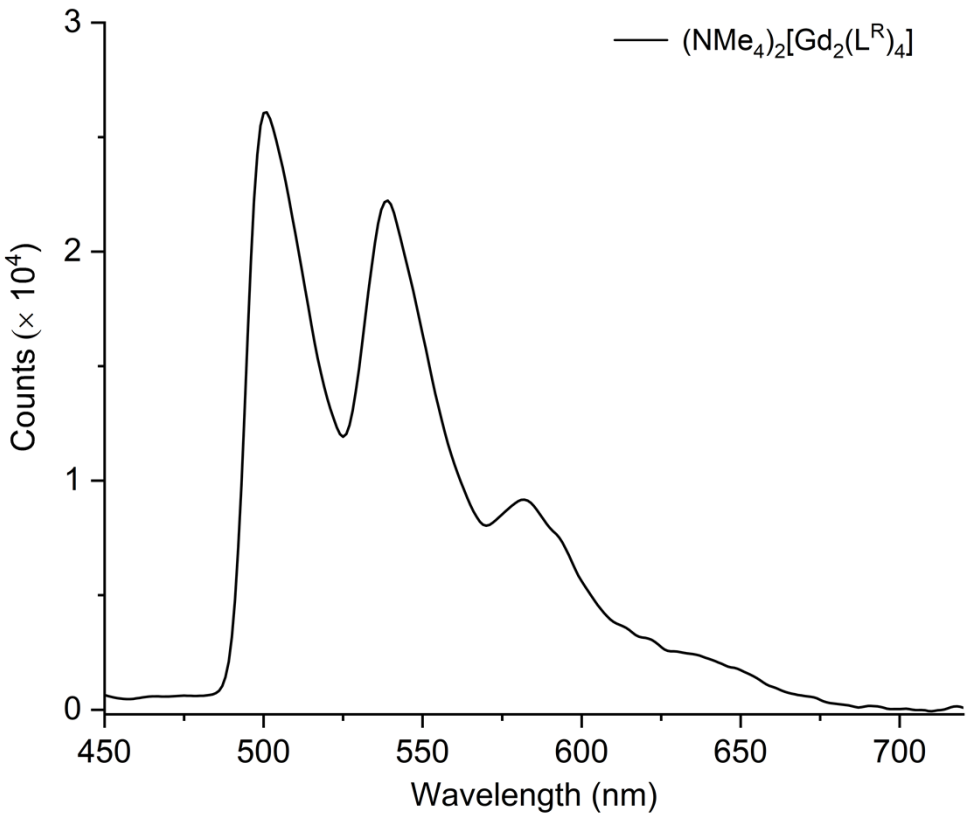

Figure S29. Phosphorescence emission spectrum of $(NMe_4)_2[Gd_2(\mathbf{L^R})_4]$ in THF.

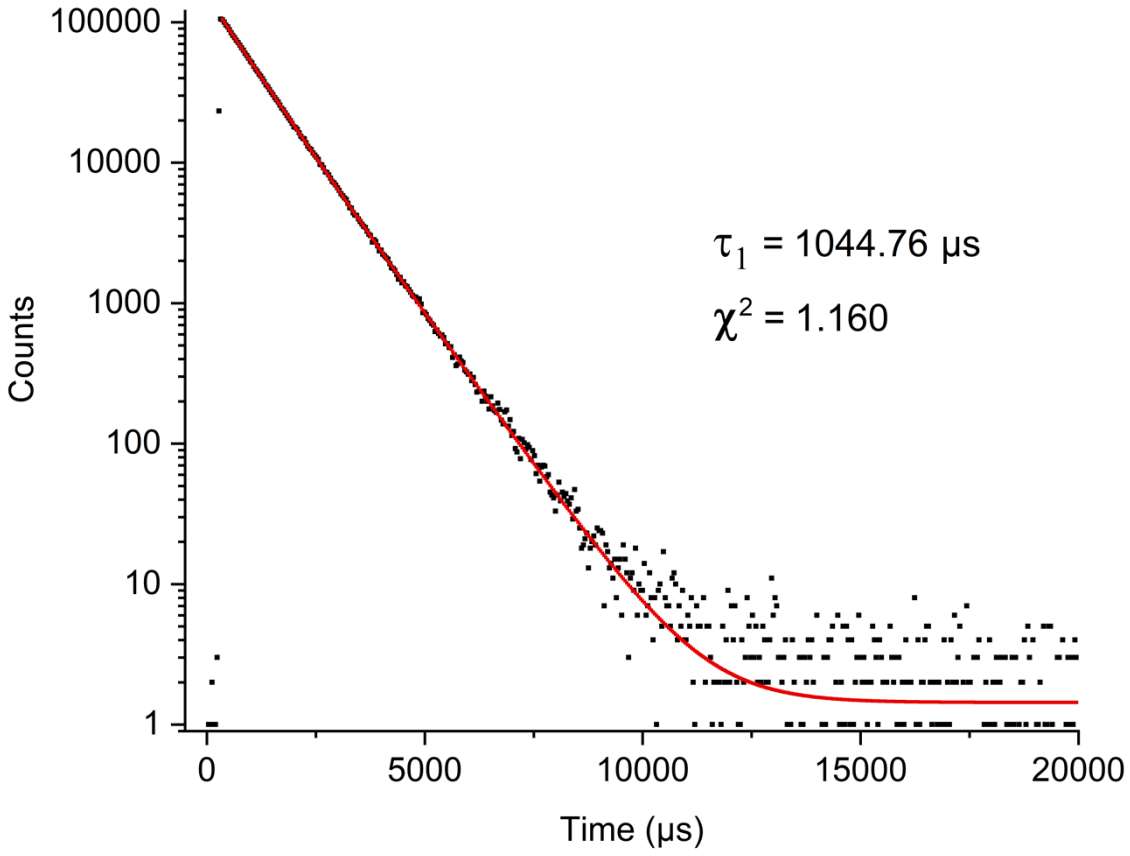

Figure S30. Luminescence decay curve of $(NMe_4)_2[Eu_2(\mathbf{L^R})_4]$ in CH_3CN (c = 2.5 × 10^{-6} M) monitored at 612 nm.

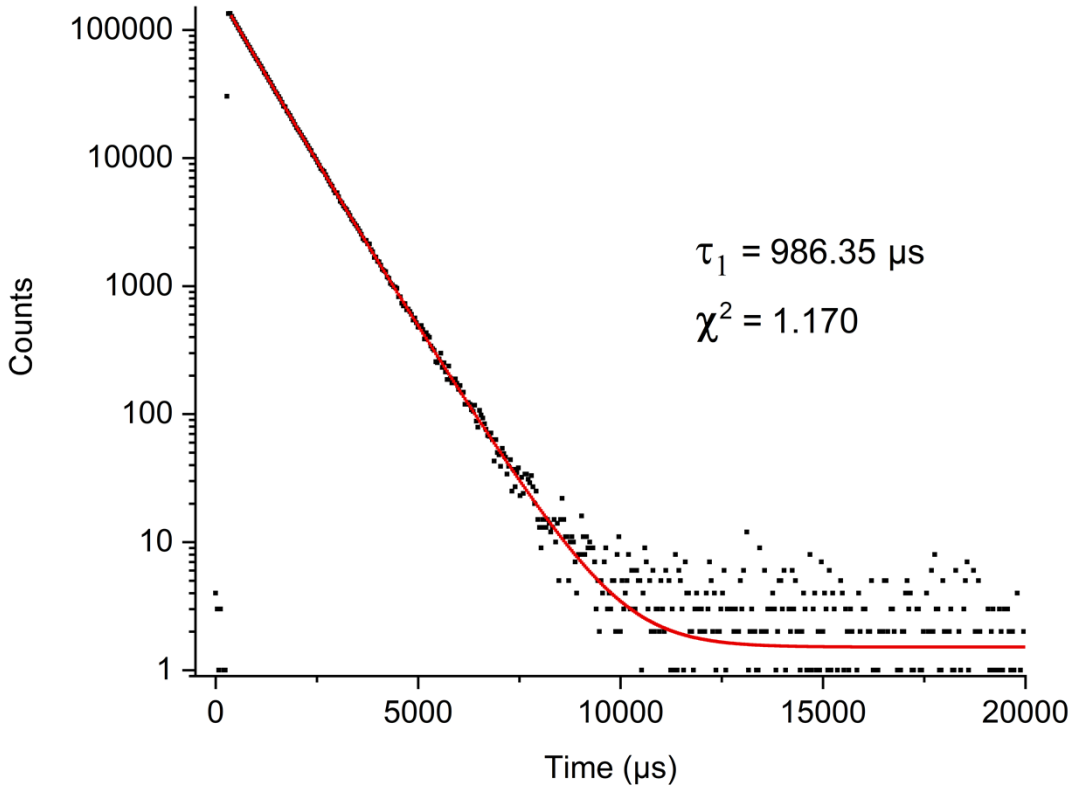

Figure S31. Luminescence decay curve of $(NMe_4)_2[Eu_2(\mathbf{L}^{S})_4]$ in $CH_3CN/CHCl_3$ = 1:9 (v/v, $c = 2.5 \times 10^{-6}$ M) monitored at 612 nm.

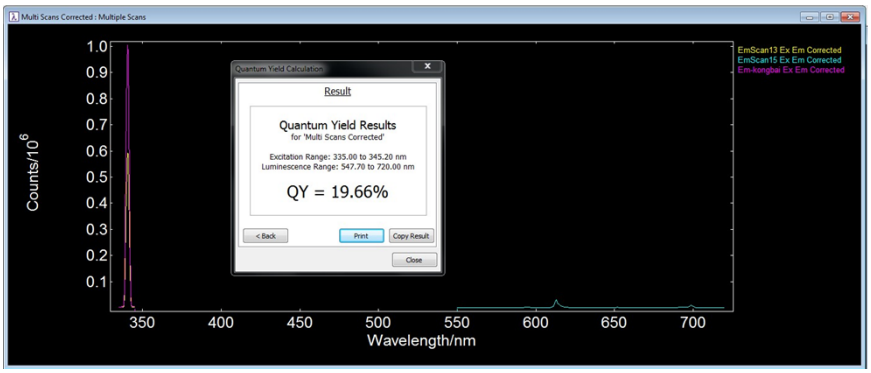

Figure S32. The screenshots of the luminescence quantum yields of $(NMe_4)_2[Eu_2(\mathbf{L}^{R})_4]$ in CH_3CN.

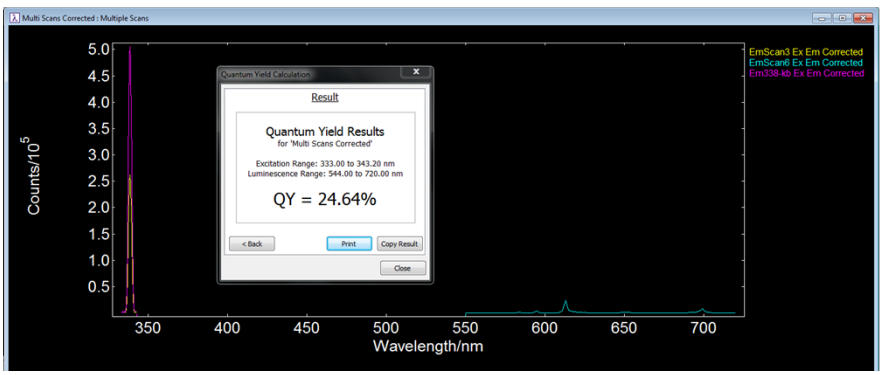

Figure S33. The screenshots of the luminescence quantum yields of $(NMe_4)_2[Eu_2(\mathbf{L}^{S})_4]$ in $CH_3CN/CHCl_3$ = 1:9 (v/v).

Table S1. Radiative (k_r) and nonradiative (k_{nr}) decay rates, observed luminescence lifetime of Eu^{3+} (τ_{obs}), intrinsic quantum yield (Φ_{Eu}), sensitization efficiency (η_{sens}) and quantum yield of Eu^{3+} ($\Phi_{overall}$). Error in τ_{obs}: ±0.05 ms; 10% relative error in the other values; λ_{ex} = 340 nm. g_{lum} values for $^5D_0 \rightarrow {}^7F_J$ of Eu^{3+} ion.

Complex	CH_3CN /$CHCl_3$ (v/v)	k_r (s^{-1})	k_{nr} (s^{-1})	Φ_{Ln} (%)	η_{sens} (%)	$\Phi_{overall}$ (%)	g_{lum} $^5D_0 \rightarrow {}^7F_J$ (J = 1, 2, 3, 4)			
							J = 1	J = 2	J = 3	J = 4
$(NMe_4)_2[Eu_2(\mathbf{L^R})_4]$	10:0	287	889	24.4	80.7	19.7	−0.233	0.039	−0.028	−0.001
	1:9	419	593	41.4	59.4	24.6	0.440	−0.076	0.115	0.011

3. Calculation of $(NMe_4)_2[Eu_2(L^R)_4]$

3.1 Cavity volume calculation of ΔΔ-$(NMe_4)_2[Eu_2(L^R)_4]$

To determine the available void space within the helicate of ΔΔ-$(NMe_4)_2[Eu_2(\mathbf{L^R})_4]$, MoloVol calculations based on the crystal structure obtained in this study was performed. The cavity volume was calculated to be 217 $Å^3$ using the parameters tabulated below. The corresponding graphics were generated with Pymol.[13]

Probe mode: two probes

Small probe radius: 1.2 Å

Large probe radius: 3 Å

Grid resolution: 0.1 Å

Optimization depth: 4

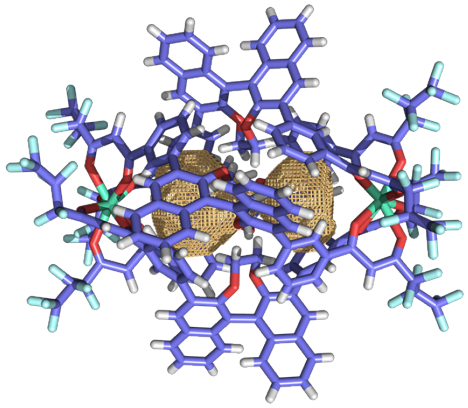

Figure S34. Cavity volumes of ΔΔ-$(NMe_4)_2[Eu_2(\mathbf{L^R})_4]$.

3.2 Hirshfeld surfaces of ΛΛ-$(NMe_4)_2[Eu_2(L^R)_4]$ and ΔΔ-$(NMe_4)_2[Eu_2(L^R)_4]$

The Hirshfeld surface highlights the supramolecular interactions of ΛΛ-$(NMe_4)[Eu_2(\mathbf{L^R})_4]^-$ and ΔΔ-$(NMe_4)[Eu_2(\mathbf{L^R})_4]^-$ with $(NMe_4)^+$. The Hirshfeld surface and fingerprint plots for ΛΛ-$(NMe_4)[Eu_2(\mathbf{L^R})_4]^-$ and ΔΔ-$(NMe_4)[Eu_2(\mathbf{L^R})_4]^-$ are shown in Figures S35−36. For the external $(NMe_4)^+$, the Hirshfeld surface analysis showed that the intermolecular force was dominated by the C−H···F interactions (i.e., H···F contacts) between the $(NMe_4)^+$ and the fluoroalkyl chains of the helicate, which accounted for 79.14% and 74.45% in ΛΛ-$(NMe_4)[Eu_2(\mathbf{L^R})_4]^-$ and ΔΔ-$(NMe_4)[Eu_2(\mathbf{L^R})_4]^-$, respectively. Subsequently, the C−H···O interactions (i.e., H···O contacts) emerge as the second prominent interactions, comprising 20.86% and 25.55% for ΛΛ-

$(NMe_4)[Eu_2(\mathbf{L^R})_4]^-$ and ΔΔ-$(NMe_4)[Eu_2(\mathbf{L^R})_4]^-$, respectively, as shown in Figure S35. In addition, for the internal $(NMe_4)^+$, Hirshfeld surface analysis showed that the intermolecular force was dominated by H···H contact, which accounted for 56.97% and 63.25% in ΛΛ-$(NMe_4)[Eu_2(\mathbf{L^R})_4]^-$ and ΔΔ-$(NMe_4)[Eu_2(\mathbf{L^R})_4]^-$, respectively. Subsequently, the C–H···π interactions (i.e., H···C contacts) emerge as the second prominent interactions, comprising 28.07% and 21.87% for ΛΛ-$(NMe_4)[Eu_2(\mathbf{L^R})_4]^-$ and ΔΔ-$(NMe_4)[Eu_2(\mathbf{L^R})_4]^-$ respectively. The C–H···O interaction (i.e., H···O contacts) accounts for 14.96% and 14.88% in ΛΛ-$(NMe_4)[Eu_2(\mathbf{L^R})_4]^-$ and ΔΔ-$(NMe_4)[Eu_2(\mathbf{L^R})_4]^-$, respectively (Figure S36).

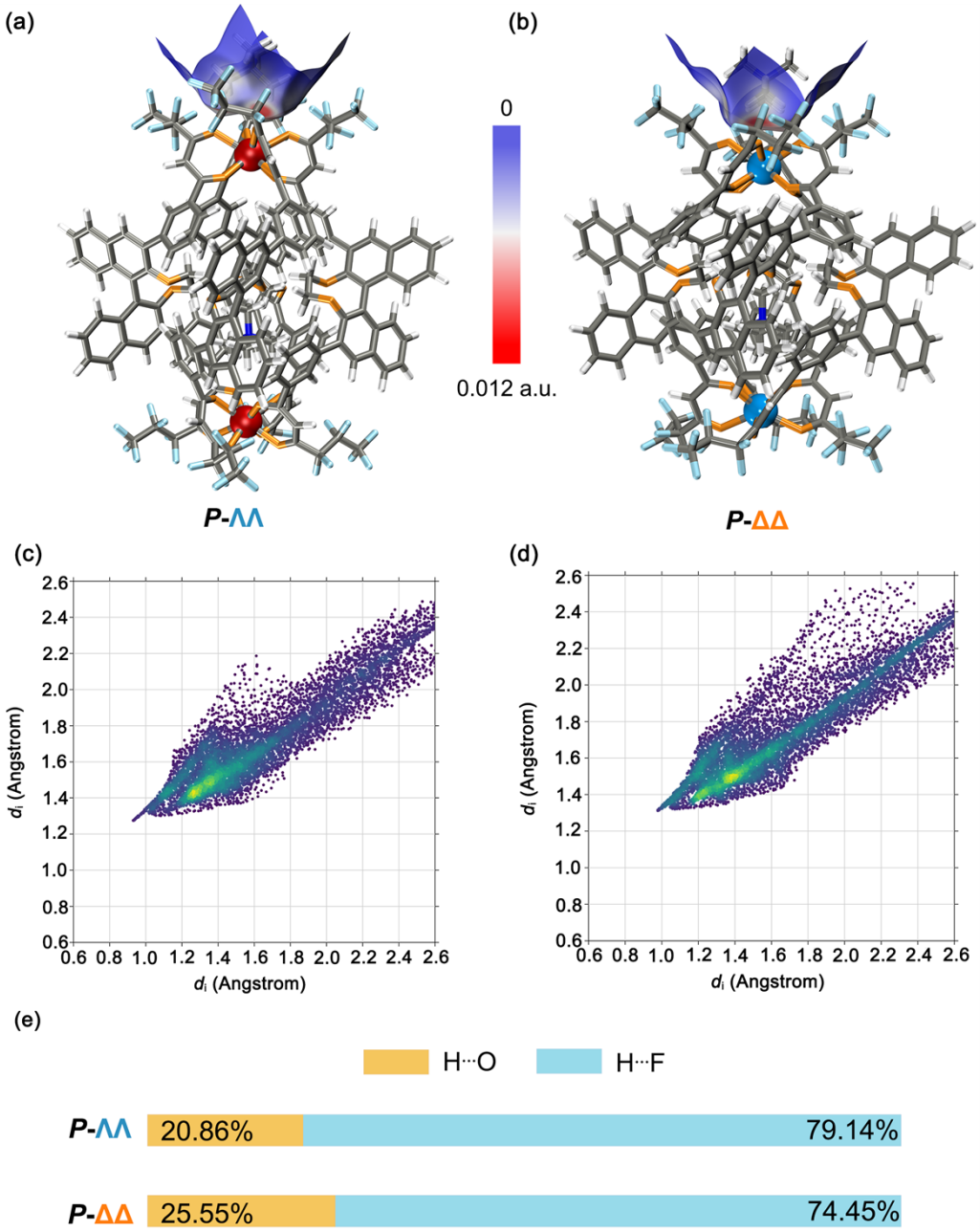

Figure S35. (a, b) Hirshfeld surfaces of ΛΛ-$(NMe_4)_2[Eu_2(\mathbf{L^R})_4]$ and ΔΔ-$(NMe_4)_2[Eu_2(\mathbf{L^R})_4]$. (c, d) 2D fingerprint plots for ΛΛ-$(NMe_4)_2[Eu_2(\mathbf{L^R})_4]$ and ΔΔ-$(NMe_4)_2[Eu_2(\mathbf{L^R})_4]$. (e) Percentage contributions of the average interactions for ΛΛ-$(NMe_4)_2[Eu_2(\mathbf{L^R})_4]$ and ΔΔ-$(NMe_4)_2[Eu_2(\mathbf{L^R})_4]$. [For ΛΛ-$(NMe_4)_2[Eu_2(\mathbf{L^R})_4]$, H···O 20.86%, H···F 79.14%; for ΔΔ-$(NMe_4)_2[Eu_2(\mathbf{L^R})_4]$, H···O 25.55%, H···F 74.45%].

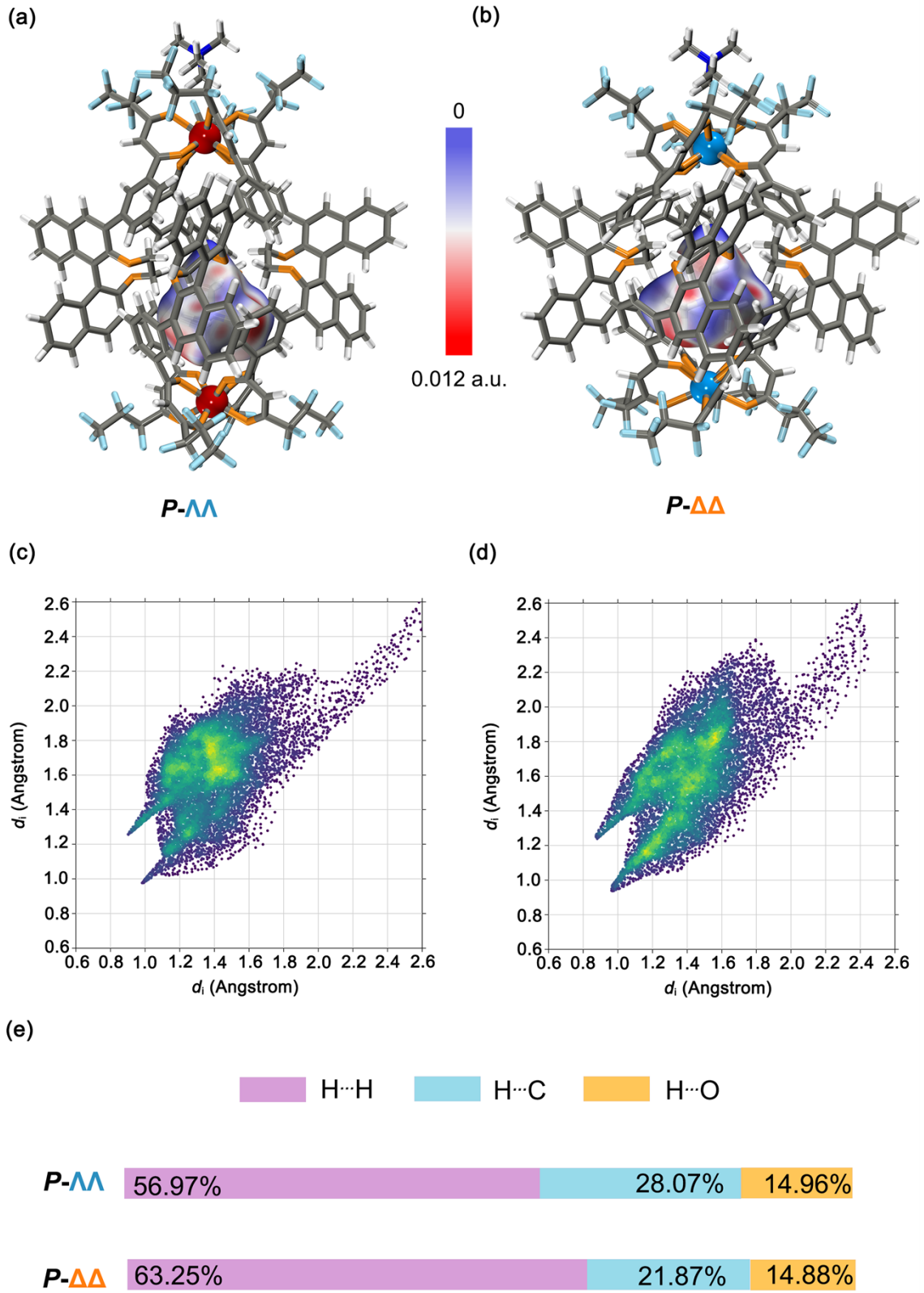

Figure S36. (a, b) Hirshfeld surfaces of ΛΛ-$(NMe_4)_2[Eu_2(\mathbf{L^R})_4]$ and ΔΔ-$(NMe_4)_2[Eu_2(\mathbf{L^R})_4]$. (c, d) 2D fingerprint plots for ΛΛ-$(NMe_4)_2[Eu_2(\mathbf{L^R})_4]$ and ΔΔ-$(NMe_4)_2[Eu_2(\mathbf{L^R})_4]$. (e) Percentage contributions of the average interactions for ΛΛ-$(NMe_4)_2[Eu_2(\mathbf{L^R})_4]$ and ΔΔ-$(NMe_4)_2[Eu_2(\mathbf{L^R})_4]$. [For ΛΛ-$(NMe_4)_2[Eu_2(\mathbf{L^R})_4]$, H···H 56.97%, H···C 28.07%, H···O 14.96%; for ΔΔ-$(NMe_4)_2[Eu_2(\mathbf{L^R})_4]$, H···H 63.25%, H···C 21.87%, H···O 14.88%].

3.3 DFT calculation of $[Eu_2(L^R)_4]^{2-}$ and $(NMe_4)_2[Eu_2(L^R)_4]$

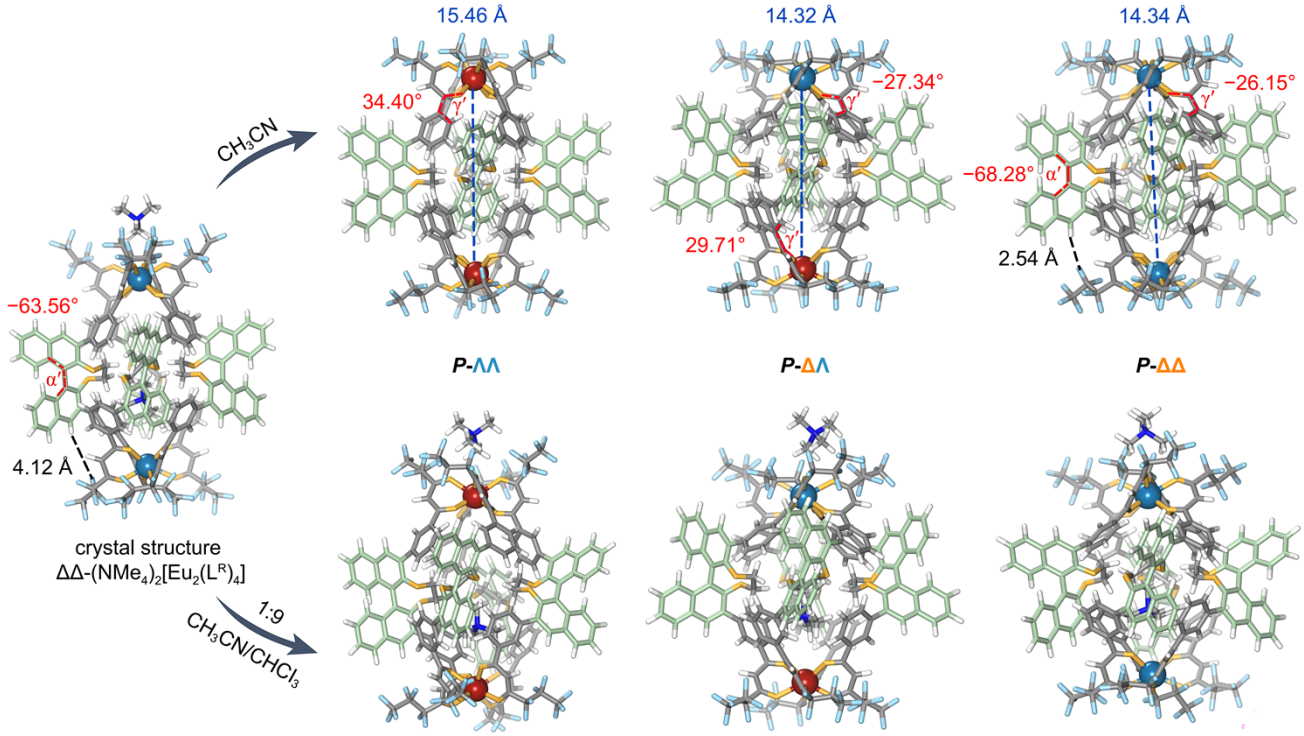

Figure S37. Crystal structure of ΔΔ-$(NMe_4)_2[Eu_2(\mathbf{L^R})_4]$ and DFT-optimized structures of ΔΔ-$[Eu_2(\mathbf{L^R})_4]^{2-}$, ΔΛ-$[Eu_2(\mathbf{L^R})_4]^{2-}$ and ΛΛ-$[Eu_2(\mathbf{L^R})_4]^{2-}$ in CH_3CN and ΔΔ-$(NMe_4)_2[Eu_2(\mathbf{L^R})_4]$, ΔΛ-$(NMe_4)_2[Eu_2(\mathbf{L^R})_4]$ and ΛΛ-$(NMe_4)_2[Eu_2(\mathbf{L^R})_4]$ in $CH_3CN/CHCl_3$ = 1:9 (v/v).

3.4 TD-DFT calculation of $(NMe_4)_2[Eu_2(L^R)_4]$

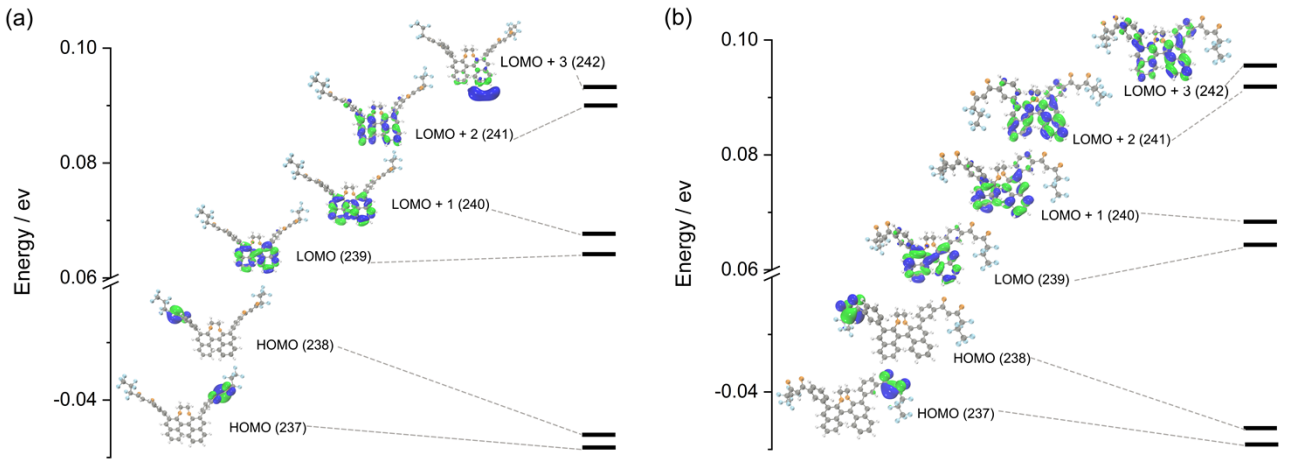

Figure S38. the electronic structure of the chromophore (ground and excited states) of (a) ΔΔ-$(NMe_4)_2[Eu_2(\mathbf{L^R})_4]$ and (b) ΛΛ-$(NMe_4)_2[Eu_2(\mathbf{L^R})_4]$ ligands.

Electron excitation analysis of ligands [ΛΛ-$(NMe_4)_2[Eu_2(\mathbf{L^R})_4]$]

Orbital 238 is HOMO, energy: −0.046951 a.u. −1.277594 eV
Orbital 239 is LUMO, energy: 0.063923 a.u. 1.739435 eV

HOMO-LUMO gap: 0.110874 a.u. 3.017030 eV 291.099160 kJ/mol
Orb: 237 Ene(au/eV): −0.048437 −1.3180 Occ: 2.000000 Type:A+B
Orb: 238 Ene(au/eV): −0.046951 −1.2776 Occ: 2.000000 Type:A+B
Orb: 239 Ene(au/eV): 0.063923 1.7394 Occ: 0.000000 Type:A+B
Orb: 240 Ene(au/eV): 0.068432 1.8621 Occ: 0.000000 Type:A+B
Orb: 241 Ene(au/eV): 0.089726 2.4416 Occ: 0.000000 Type:A+B
Orb: 242 Ene(au/eV): 0.094260 2.5649 Occ: 0.000000 Type:A+B

Some MO transitions sorted by absolute contributions:
1052 238 −> 239 Coeff.: 0.64651 Contri.: 83.5950%
1053 238 −> 240 Coeff.: 0.28041 Contri.: 15.7260%
1054 238 −> 241 Coeff.: −0.02747 Contri.: 0.1509%
1056 238 −> 243 Coeff.: −0.02449 Contri.: 0.1200%
1066 238 −> 254 Coeff.: 0.01804 Contri.: 0.0651%
1067 238 −> 255 Coeff.: −0.01803 Contri.: 0.0650%
1068 238 −> 256 Coeff.: 0.01625 Contri.: 0.0528%
1065 238 −> 253 Coeff.: −0.01376 Contri.: 0.0379%
1059 238 −> 246 Coeff.: 0.01163 Contri.: 0.0271%
1071 238 −> 259 Coeff.: 0.01045 Contri.: 0.0218%

Some MO transitions sorted by absolute contributions:
1050 238 -> 239 Coeff.: 0.64682 Contri.: 83.6752%
1051 238 −> 240 Coeff.: 0.27968 Contri.: 15.6442%
1052 238 −> 241 Coeff.: 0.02752 Contri.: 0.1515%
1054 238 −> 243 Coeff.: 0.02447 Contri.: 0.1198%
1065 238 −> 255 Coeff.: 0.01802 Contri.: 0.0649%
1064 238 −> 254 Coeff.: 0.01798 Contri.: 0.0647%
1066 238 −> 256 Coeff.: −0.01629 Contri.: 0.0531%
1063 238 −> 253 Coeff.: 0.01380 Contri.: 0.0381%
1057 238 −> 246 Coeff.: −0.01162 Contri.: 0.0270%
1069 238 −> 259 Coeff.: −0.01045 Contri.: 0.0218%

Electron excitation analysis of ligands [ΔΔ-$(NMe_4)_2[Eu_2(L^R)_4]$]
Orbital 238 is HOMO, energy: −0.047678 a.u. −1.297396 eV
Orbital 239 is LUMO, energy: 0.065679 a.u. 1.787216 eV
HOMO-LUMO gap: 0.113357 a.u. 3.084611 eV 297.619799 kJ/mol

Orb: 237 Ene(au/eV): −0.049252 −1.3402 Occ: 2.000000 Type:A+B
Orb: 238 Ene(au/eV): −0.047678 −1.2974 Occ: 2.000000 Type:A+B
Orb: 239 Ene(au/eV): 0.065679 1.7872 Occ: 0.000000 Type:A+B
Orb: 240 Ene(au/eV): 0.070031 1.9056 Occ: 0.000000 Type:A+B
Orb: 241 Ene(au/eV): 0.092063 2.5052 Occ: 0.000000 Type:A+B
Orb: 242 Ene(au/eV): 0.096106 2.6152 Occ: 0.000000 Type:A+B

Some MO transitions sorted by absolute contributions:

1371	238 –>	239	Coeff.:	0.64238	Contri.:	82.5304%
1372	238 –>	240	Coeff.:	0.28738	Contri.:	16.5175%
1373	238 –>	241	Coeff.:	0.03371	Contri.:	0.2273%
1374	238 –>	242	Coeff.:	−0.03224	Contri.:	0.2079%
1383	238 –>	251	Coeff.:	−0.02418	Contri.:	0.1169%
1382	238 –>	250	Coeff.:	0.01585	Contri.:	0.0502%
1384	238 –>	252	Coeff.:	0.01546	Contri.:	0.0478%
1386	238 –>	254	Coeff.:	−0.01471	Contri.:	0.0433%
1127	236 –>	245	Coeff.:	0.01163	Contri.:	0.0271%
1381	238 –>	249	Coeff.:	−0.01151	Contri.:	0.0265%

Some MO transitions sorted by absolute contributions:

1342	238 –>	239	Coeff.:	0.64052	Contri.:	82.0532%
1343	238 –>	240	Coeff.:	0.29143	Contri.:	16.9863%
1344	238 –>	241	Coeff.:	0.03360	Contri.:	0.2258%
1345	238 –>	242	Coeff.:	−0.03274	Contri.:	0.2144%
1354	238 –>	251	Coeff.:	−0.02468	Contri.:	0.1218%
1353	238 –>	250	Coeff.:	0.01579	Contri.:	0.0499%
1357	238 –>	254	Coeff.:	−0.01509	Contri.:	0.0455%
1355	238 –>	252	Coeff.:	0.01483	Contri.:	0.0440%
1352	238 –>	249	Coeff.:	−0.01172	Contri.:	0.0275%
1102	236 –>	245	Coeff.:	0.01142	Contri.:	0.0261%

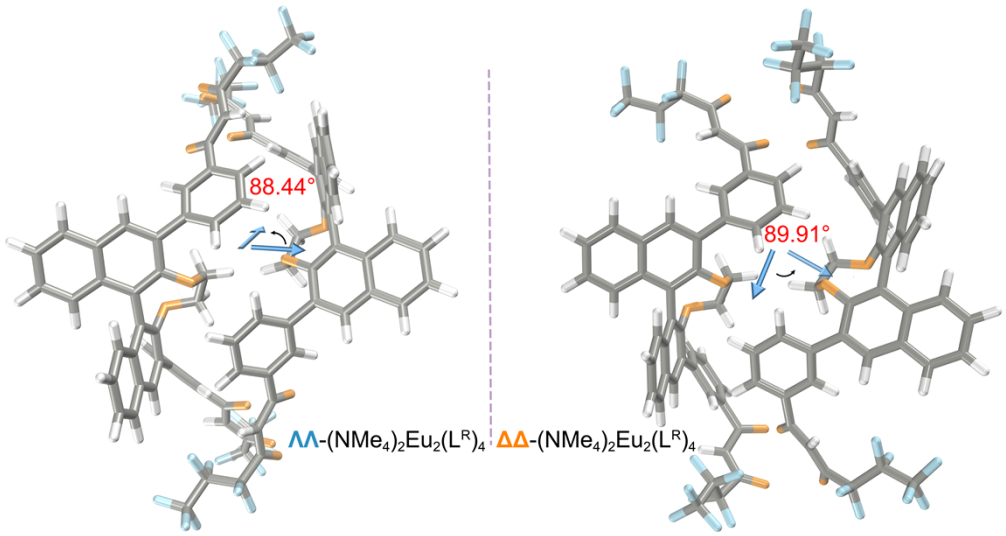

Figure S39. the calculated transition dipole of ΛΛ-$(NMe_4)_2[Eu_2(\mathbf{L^R})_4]$ and (b) ΔΔ-$(NMe_4)_2[Eu_2(\mathbf{L^R})_4]$ ligands.

The Geometry center and Fragment transition dipole moment are listed below.

Geometry center:

−0.02844434417784214 −1.783811330795288 2.6841776371002197

Fragment transition dipole moment:

−0.02829700000000002 0.008912000000000031 −0.09150400000000002

Geometry center:

−0.028144370764493942 2.6836326122283936 1.7850556373596191

Fragment transition dipole moment:

0.028307000000000044 0.091361 0.008900999999999895

Geometry center:

0.05084468051791191 2.5690112113952637 4.452744483947754

Fragment transition dipole moment:

0.19646300000000003 0.06938600000000002 −0.05748599999999994

Geometry center:

0.062144502997398376 4.45693302154541 −2.565377950668335

Fragment transition dipole moment:

0.1925560000000001 −0.058370000000000054 −0.06752599999999996

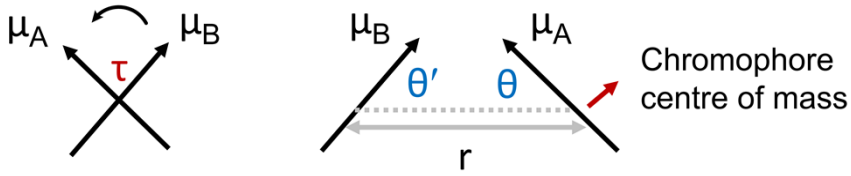

Figure S40. Geometrical parameters used to define the orientation of two transition dipole moments.

τ is the angle between μ_A and μ_B if their centres of mass are superimposed, θ is the angle between μ_A and $\hat{r}$, and θ′ is the angle -between μ_B and $\hat{r}$, where $\hat{r}$ is the vector connecting the centres of gravity of the chromophores and r is the length of this vector.

The sign and magnitude of the Cotton effects that comprise an exciton couplet are defined by rotational strengths (R^A and R^B),[14] the CD equivalent of oscillator strengths in linear absorption spectroscopy, which are given by Eqn (S5):

$$R^{A/B} = \pm \frac{E\mu^2 r}{4\hbar}(\sin\theta \cdot \sin\theta' \cdot \sin\tau) \qquad (S5)$$

Here τ is defined as the anticlockwise dihedral angle between the two dipole moments, and E is the energy of the transition from the ground state to the unperturbed excited state (X).

Table S2. The transition dipole included angle (τ) and the angle (θ/θ′) between μ_A/μ_B and $\hat{r}$.

	θ (deg)	θ′ (deg)	τ (deg)
ΛΛ-$(NMe_4)_2[Eu_2(\mathbf{L}^R)_4]$	45.76	45.80	88.44
ΔΔ-$(NMe_4)_2[Eu_2(\mathbf{L}^R)_4]$	44.07	46.01	89.91

4. Coordination polyhedra and X-ray crystallography of ΔΔ-$(NMe_4)_2Eu_2(L^R)_4$

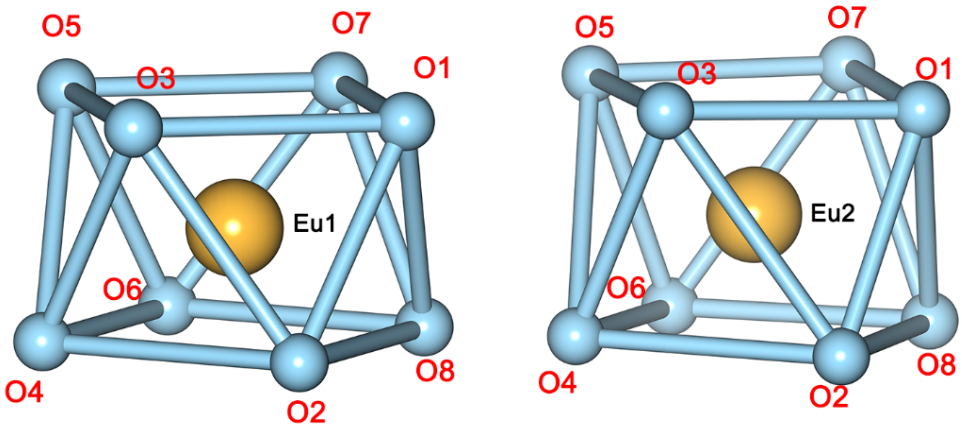

Figure S41. Coordination polyhedra of ΔΔ-$(NMe_4)_2[Eu_2(\mathbf{L^R})_4]$ (Eu1 and Eu2).

Table S3. Shape analysis of ΔΔ-$(NMe_4)_2[Eu_2(\mathbf{L^R})_4]$ using SHAPE 2.1 software.

Helicate	Square antiprism	Biaugmented trigonal prism	Triangular dodecahedron
ΔΔ-$(NMe_4)_2[Eu_2(\mathbf{L^R})_4]$ (Eu1)	0.475	1.892	2.585
ΔΔ-$(NMe_4)_2[Eu_2(\mathbf{L^R})_4]$ (Eu2)	0.186	2.158	2.535

Table S4. Crystal data of ΔΔ-$(NMe_4)_2[Eu_2(\mathbf{L^R})_4]$.

	$(NMe_4)_2[Eu_2(\mathbf{L^R})_4]$
CCDC Number	2353626
Empirical formula	$C_{196}H_{136}Eu_2F_{56}N_3O_{24}$
Formula weight	4284.99
Color	Colorless
Crystal System	tetragonal
Space group	$P42_12$
a (Å)	23.1516 (7)
b (Å)	23.1516 (7)
c (Å)	24.2797 (10)
α (deg)	90
β (deg)	90
γ (deg)	90
V (Å^3)	13013.8 (10)
Z	2
ρ (g cm^3)	1.094
μ (mm^{-1})	0.566
F (000)	4310.0
R_1, [$I > 2\sigma$ (I)]	0.1583
wR_2, [$I > 2\sigma$ (I)]	0.4079
R_1, (all data)	0.2181
wR_2, (all data)	0.4423
GOF on F^2	1.356

5. References

[1] G. M. Sheldrick, Crystal structure refinement with SHELXL, *Acta Crystallogr. Sect. C-Struct. Chem.*, 2015, **71**, 3−8.

[2] O. V. Dolomanov, L. J. Bourhis, R. J. Gildea, J. A. K. Howard and H. Puschmann, OLEX2: a complete structure solution, refinement and analysis program, *J. Appl. Crystallogr.*, 2009, **42**, 339−341.

[3] DFT calculations were performed using Gaussian16, revisionC.01; M. J. Frisch, G. W. Trucks, H. B. Schlegel, G. E. Scuseria, M. A. Robb, J. R. Cheeseman, G. Scalmani, V. Barone, G. A. Petersson, H. Nakatsuji, X. Li, M. Caricato, A. V. Marenich, J. Bloino, B. G. Janesko, R. Gomperts, B. Mennucci, H. P. Hratchian, J. V. Ortiz, A. F. Izmaylov, J. L. Sonnenberg,D. Williams-Young, F. Ding, F. Lipparini, F. Egidi, J. Goings, B. Peng, A. Petrone, T. Henderson, D. Ranasinghe, V. G. Zakrzewski, J. Gao, N. Rega, G. Zheng, W. Liang, M. Hada, M. Ehara, K. Toyota, R. Fukuda, J. Hasegawa, M. Ishida, T. Nakajima, Y. Honda, O. Kitao, H. Nakai, T. Vreven, K. Throssell, J. A. Montgomery, Jr., J. E. Peralta, F. Ogliaro, M. J. Bearpark, J. J. Heyd, E. N. Brothers, K. N. Kudin, V. N. Staroverov, T. A. Keith, R. Kobayashi, J. Normand, K. Raghavachari, A. P. Rendell, J. C. Burant, S. S. Iyengar, J. Tomasi, M. Cossi, J. M. Millam, M. Klene, C. Adamo, R. Cammi, J. W. Ochterski, R. L. Martin, K. Morokuma, O. Farkas, J. B. Foresman and D. J. Fox, Gaussian, Inc.: Wallingford CT, 2016.

[4] S. Grimme, S. Ehrlich and L. Goerigk, Effect of the damping function in dispersion corrected density functional theory, *J. CoSSmput. Chem.*, 2011, **32**, 1456−1465.

[5] M. Dolg, U. Wedig, H. Stoll and H. Preuss, Energyadjusted ab initio pseudopotentials for the first row transition elements, *J. Chem. Phys.*, 1987, **86**, 866−872.

[6] J. M. L. Martin and A. Sundermann, Correlation consistent valence basis sets for use with the Stuttgart-Dresden-Bonn relativistic effective core potentials: The atoms Ga–Kr and In–Xe, *J. Chem. Phys.*, 2001, **114**, 3408−3420.

[7] A. V. Marenich, C. J. Cramer and D. G. Truhlar, Universal solvation model based on solute electron density and on a continuum model of the solvent defined by the bulk dielectric constant and atomic surface tensions, *J. Phys. Chem. B*, 2009, **113**, 6378−6396.

[8] R. Krishnan, J. S. Binkley, R. Seeger and J. A. Pople, Selfconsistent molecular orbital methods. XX. A basis set for correlated wave functions, *J. Chem. Phys.*, 1980, **72**, 650−654.

[9] J. Zheng, X. Xu and D. G. Truhlar, Minimally augmented karlsruhe basis sets, *Theor. Chem. Acc.*, 2011, **128**, 295−305.

[10] T. Lu, F. Chen, Multiwfn: a multifunctional wavefunction analyzer, *J. Comput. Chem.*, 2012, **33**, 580−592.

[11] W. Humphrey, A. Dalke and K. Schulten, VMD: visual molecular dynamics, *J. Mol. Graphics.*, 1996, **14**, 33−38

[12] F. Romanov-Michailidis, L. Guénée and A. Alexakis, Enantioselective organocatalytic fluorination-induced wagner-meerwein rearrangement, *Angew. Chem. Int. Ed.*, 2013, **52**, 9266−9270.

[13] S. LLC and W. DeLano, 2020, Available at: http://www.pymol.org/pymol.

[14] A. Rodger and B. Norden, Circular dichroism and linear dichroism, Oxford University Press, Oxford, 1997.